Using basis sets of scar functions

F. Revuelta,[1,*] R. M. Benito,[1,†] F. Borondo,[2,‡] and E. Vergini[1,3,§]

[1]*Grupo de Sistemas Complejos and Departamento de Física, Escuela Técnica Superior de Ingenieros Agrónomos, Universidad Politécnica de Madrid, 28040 Madrid, Spain*

[2]*Departamento de Química, and Instituto de Matemáticas (ICMAT), Universidad Autónoma de Madrid, Cantoblanco, 28049 Madrid, Spain*

[3]*Departamento de Física, Comisión Nacional de Energía Atómica, Avenida del Libertador 8250, 1429 Buenos Aires, Argentina*

(Received 26 July 2012; revised manuscript received 12 March 2013; published 23 April 2013)

We present a method to efficiently compute the eigenfunctions of classically chaotic systems. The key point is the definition of a modified Gram-Schmidt procedure which selects the most suitable elements from a basis set of scar functions localized along the shortest periodic orbits of the system. In this way, one benefits from the semiclassical dynamical properties of such functions. The performance of the method is assessed by presenting an application to a quartic two-dimensional oscillator whose classical dynamics are highly chaotic. We have been able to compute the eigenfunctions of the system using a small basis set. An estimate of the basis size is obtained from the mean participation ratio. A thorough analysis of the results using different indicators, such as eigenstate reconstruction in the local representation, scar intensities, participation ratios, and error bounds, is also presented.

DOI: 10.1103/PhysRevE.87.042921 PACS number(s): 05.45.Mt, 03.65.Sq

I. INTRODUCTION

The vast majority of methods to obtain quantum stationary states rely on the expansion of the corresponding wave functions in a basis set of suitable basis functions that can be made (approximately) complete, on which the Hamiltonian of the system is diagonalized. The choice of the basis set is then critical for the efficiency of the method. This issue is particularly important in the case of heavy-particle dynamics or in the semiclassical limit, where these functions oscillate considerably. The situation is even worse for very chaotic or ergodic systems, such as those in which we are interested in this paper.

Several methods have been proposed in the literature. The simplest procedure uses products of harmonic oscillator eigenfunctions, something which works well to describe a good number of low-lying states but gets progressively poor as energy increases due to anharmonicities (see, for example, Refs. [1,2]. Going to the other extreme, other methods have been proposed making use of the semiclassical information derived from quantized invariant classical structures [3], which render excellent results [4,5].

In this paper we investigate the feasibility of using scar functions, localized over short periodic orbits (POs), as a basis set to efficiently compute the eigenstates of classically chaotic Hamiltonian systems. The term "scar" was introduced by Heller in a seminal paper [6] to describe the dramatic enhancement of quantum probability density that takes place along POs in some eigenfunctions of the Bunimovich stadium billiard, as a result of the recurrences along the scarring orbit. The relevance of unstable POs in the quantization of classically chaotic systems had been previously pointed out by Gutzwiller in his celebrated trace formula (GTF) [7]. Other fundamental contributions to the theory of scars [8] were made by Bogomolny [9], who showed how this extra density is obtained by averaging in configuration space groups of eigenfunctions in an energy window around Bohr-Sommerfeld (BS) quantized energies in the $\hbar \to 0$ limit. The corresponding phase-space version using Wigner functions was investigated by Berry [10]. Other interesting aspects of scarring, such as the role of homoclinic and heteroclinic quantized circuits [11,12], the influence of bifurcations (in systems with mixed dynamics) [13], the scarring of individual resonance eigenstates in open systems [14], and relativistic scarring [15], have also been discussed in the literature. Scars have also been experimentally observed in many different contexts, including microwave cavities [16], semiconductor nanodevices [17], optical microcavities [18], optical fibers [19], and graphene sheets [20].

Different methods have been described in the literature to systematically construct functions localized on unstable POs (hereafter called scar functions). Polavieja *et al*. averaged groups of eigenstates using the short-time true quantum dynamics of the system [21]. Vergini and coworkers used the short PO theory [22] and obtained scar functions by combination of resonances of POs over which the condition of minimum energy dispersion is imposed, thus including the semiclassical dynamics around the scarring PO up to the Ehrenfest time [23]. Sibert *et al*. [24] and Revuelta *et al*. [25] extended the method to smooth potential systems. Also, Vagog *et al*. extend to unstable POs the asymptotic boundary layer method to calculate stable microresonator localized modes [26]. These scar functions not only appear well localized in configuration and phase space, but also present a very low dispersion in energy [27], and this property makes them good candidates *a priori* to form an efficient basis set for calculation of the eigenstates of classically chaotic systems. An additional advantage of using this kind of basis functions, which are based on dynamical information, is that they should allow easy and straightforward identification of the underlying invariant classical structures that are relevant for the semiclassical description of individual states of a chaotic system.

In this paper we introduce a new method to construct basis sets formed by the scar functions described before [23–25]

*fabio.revuelta@upm.es
†rosamaria.benito@upm.es
‡f.borondo@uam.es
§vergini@tandar.cnea.gov.ar

that can be used to efficiently compute the eigenvalues and eigenfunctions of classically chaotic systems with smooth potentials.

This method exploits a simple semiclassical idea, based on the well-known Weyl law for closed systems, which gives an intuitive explanation of how the quantum states of a system "fill" the corresponding phase space [3]. Put in numerical terms, the associated volume divided by that of a Planck cell (that taken by a single state) gives a semiclassical estimation of the generated Hilbert space size,

$$N_{\mathcal{E}} = \frac{\int\int d\mathbf{p}d\mathbf{q}\Theta[\mathcal{E} - \mathcal{H}(\mathbf{p},\mathbf{q})]}{(2\pi\hbar)^d},$$

where d is the dimensionality of the problem, and Θ the Heaviside function. The application of this prescription, i.e., the calculation of the phase-space integral in the above expression, is particularly simple when one aims at calculating all states up to a given energy, $\mathcal{E}$, which then provides an easy way to compute a minimum bound to the dimension of the required basis set. Obviously, it is always advisable to increase this number a little bit to account for the border effects, in order to obtain a better description of the states localized in this region of phase space. This type of strategy has long been proposed in the literature. For example, Heller *et al*. [5] choose to fill the relevant phase space up to the considered energy with coherent states or linear superpositions of such states placed along quantized trajectories. Note that the usual basis sets, constructed, for example, with (orthogonal) products of harmonic oscillator functions on each coordinate, are less efficient since they are more poorly adapted to the relevant phase space, unnecessarily extending into the classically forbidden regions. Bogomolny [4] used semiclassical functions distributed in a narrow crust around a given energy shell, thus covering a phase-space volume given by the surface of the mean energy shell times the energy width of the functions. Our method is similar in spirit to this one, and the required phase space up to a given energy is then filled up with a succession of overlying layers, one on top of each other, in an onion-like fashion. Very recently [28], basis sets of scar functions defined over short POs have been used to compute the eigenstates of the evolution operator in open quantum maps. In addition to showing a great performance for this task, they have proven to be a very powerful tool for the analysis of the behavior of these kinds of systems. The fact that our scar functions are defined with a very low energy dispersion means that they fill the phase space very effectively, i.e., with smaller basis sizes. Note that some complications arise when constructing the basis elements, due to the overlap existing among the scar functions. Finally, let us remark that the kind of basis sets proposed here can be considered optimal from a semiclassical point of view, since they minimize the dispersion by making a time evolution until Ehrenfest time [see Eq. (13) below].

The performance of the method is illustrated with an application to a highly chaotic coupled quartic oscillator with 2 degrees of freedom that has been extensively studied in connection with quantum chaos [1,2,29]. We show how our method is able to accurately compute the ∼2400 low-lying eigenfunctions of the quartic oscillator using a basis set consisting of only ∼2500 elements constructed over 18 POs of the system. Furthermore, we demonstrate that the method can be used to compute the eigenfunctons of the system in a small energy window using a basis set whose size is of the same order of magnitude as the number of computed eigenfunctions. An estimate of this basis size is obtained from the mean participation ratio, and it turns out to be much smaller than those used in other methods. The extension to systems of higher dimensionality is straightforward.

The organization of the paper is as follows. In Sec. II we introduce the system chosen for study. Section III is devoted to the description of the method that we have developed, which is based on two central or key pillars. First, we use a general procedure able to construct localized functions along unstable POs for Hamiltonian systems with smooth potentials. Second, we use a *selective* Gram-Schmidt method (SGSM) to select a linearly independent scar function subset from an overcomplete set within a given energy window, thus obtaining by direct diagonalization of the corresponding Hamiltonian matrix the desired eigenenergies and eigenfunctions with a great degree of accuracy using standard routines. We also describe in this section the different mathematical tools that are used in the analysis of the quality of our results. They are (i) local representation functions, (ii) scar intensities or the contribution of each PO to the emergence of an individual eigenfunction, and (iii) participation ratios, from which an approximated idea of the number of basis elements needed to reconstruct an eigenfunction can be obtained. In Sec. IV we present and discuss the results obtained in the calculation of the eigenstates of the system. Finally, in Sec. V we summarize the main conclusions of our work and make some final remarks.

II. SYSTEM

Our system consists of a particle of unit mass moving in a quartic potential on the x-y plane,

$$\mathcal{H}(P_x,P_y,x,y) = \frac{P_x^2 + P_y^2}{2} + \frac{x^2y^2}{2} + \frac{\beta}{4}(x^4 + y^4), \quad (1)$$

with the parameter $\beta = 1/100$. This Hamiltonian has very often been used in studies concerning quantum chaos [1,2,29,30]. A plot of the equipotential line $\mathcal{E} = 1$ is shown in Fig. 1(a). The corresponding dynamics are highly chaotic; note that no signs of invariant tori can be identified in Fig. 1(b), where the $\{y = 0, P_y > 0\}$ Poincaré surface of section (SOS) for a typical trajectory at $\mathcal{E} = 1$ is shown. However, some stable POs exist [31,32], although the areas of their stability regions are negligible for all practical purposes. Another interesting property of Hamiltonian (1) is that, due to the fact that the potential is homogeneous, it is mechanically similar. This implies that any trajectory, $(x_t, y_t, P_{x,t}, P_{y,t})$, at a given energy, $\mathcal{E}$, can be scaled to another, $(x'_{t'}, y'_{t'}, P'_{x,t'}, P'_{y,t'})$, at a different energy, $\mathcal{E}'$, by using the simple scaling relations

$$\begin{aligned} x'_{t'} &= \left(\frac{\mathcal{E}'}{\mathcal{E}}\right)^{1/4} x_t, \quad P'_{x,t'} = \left(\frac{\mathcal{E}'}{\mathcal{E}}\right)^{1/2} P_{x,t}, \\ y'_{t'} &= \left(\frac{\mathcal{E}'}{\mathcal{E}}\right)^{1/4} y_t, \quad P'_{y,t'} = \left(\frac{\mathcal{E}'}{\mathcal{E}}\right)^{1/2} P_{y,t}, \end{aligned} \quad (2)$$

where $t' = (\mathcal{E}'/\mathcal{E})^{-1/4}t$. Note that the above relations imply that the structure of the phase space is the same for all values of

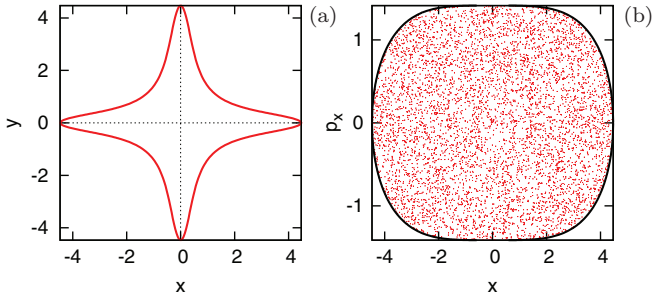

FIG. 1. (Color online) (a) Equipotential line for the quartic oscillator corresponding to $\mathcal{E} = 1$. (b) $y = 0$ with a $P_y > 0$ Poincaré surface of section for a typical trajectory of the system at $\mathcal{E} = 1$. No signs of regular motion are apparent.

the energy. Furthermore, from these expressions it can easily be shown that the classical action, $S_t = \int_0^t d\tau [P_{x,\tau}^2 + P_{y,\tau}^2]$, scales as

$$S'_{t'} = \left(\frac{\mathcal{E}'}{\mathcal{E}}\right)^{3/4} S_t. \tag{3}$$

Note that the period of a PO fulfills

$$T = \frac{3}{4}\frac{S_T}{\mathcal{E}}. \tag{4}$$

Finally, we present in Fig. 2 the 18 POs for the system described by Hamiltonian (1) that are used in the calculations in this paper. They have been chosen as the semiclassically most relevant ones, in the sense that they are short, symmetric and not too unstable (see discussion in Sec. III A2).

III. METHOD

In this section we describe the method that is used in our calculations. This description is made in three steps. First, we define the scar functions that are used to construct our basis sets. Second, we describe the procedure by which the elements of the basis set are selected and computed. And third, we introduce the mathematical tools that are used to analyze the characteristics and quality of our results.

A. The scar functions

This subsection consists of four parts. We first introduce (auxiliary) tube functions. Then some attention is paid to the details of the BS quantization procedure on the PO. In the third part, we discuss the actual calculations of the scar functions, which are obtained by dynamically improving the tube functions and constitute the primary ingredient of our basis elements. Finally, some examples of scar functions are presented and discussed.

1. The tube functions

Some auxiliary tube functions are first defined as

$$\psi_n^{\text{tube}}(x,y) = \int_0^T dt e^{i\mathcal{E}_n t/\hbar} \phi(x,y,t), \tag{5}$$

where T is the period of the PO, and $\mathcal{E}_n$ is the associated BS quantized energy (see Sec. III A2). The wave function $\phi(x,y,t)$

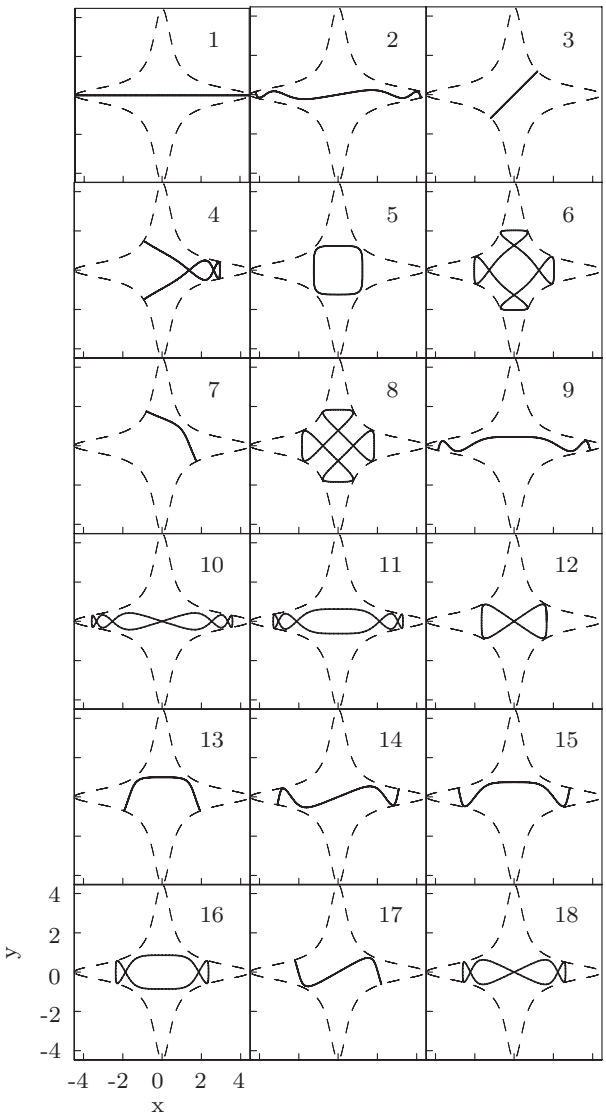

FIG. 2. Unstable periodic orbits for the quartic oscillator, (1), at energy $\mathcal{E} = 1$ relevant for this work. The corresponding equipotential line is also shown, by the dashed line.

is a suitable wave packet, whose dynamics is forced to stay in the neighborhood of the scarring PO, $(x_t, y_t, P_{x,t}, P_{y,t})$. For this purpose, we use a frozen Gaussian [33,34] centered on the trajectory, which can be expressed as

$$\begin{aligned}\phi(x,y,t) = \exp\{&-\alpha_x(x-x_t)^2 - \alpha_y(y-y_t)^2 \\ &+ (i/\hbar)[P_{x,t}(x-x_t) + P_{y,t}(y-y_t)] + i\gamma_t\},\end{aligned} \tag{6}$$

where α_x and α_y define the widths along the two axes. In our calculation we take, for simplicity, $\alpha_x = \alpha_y = 1$, which is an adequate value for the problem that we are considering here. The phase

$$\begin{aligned}\gamma_t &= \frac{1}{\hbar}\int_0^t d\tau \left(P_{x,\tau}^2 + P_{y,\tau}^2\right) - \frac{\pi}{2}\mu_t \\ &= \frac{S_t}{\hbar} - \frac{\pi}{2}\mu_t\end{aligned} \tag{7}$$

is the difference between the dynamical phase of the orbit [cf. Eq. (3)] and a topological phase, proportional to the

function μ_t, which can be calculated by applying Floquet's theorem [35]. For this purpose, the transversal motion is decomposed in the vicinity of a PO into two terms: one purely hyperbolic, describing the dilatation-contraction that takes place along the directions of the associated invariant manifolds; and the other, periodic in time, which is described by the matrix $F(t)$ introduced in Eq. (11) of Ref. [23]. After one period of time, $\mu_T \equiv \mu$ is given by the winding number of the PO, which equals the number of half-turns made by the manifold directions as they move along the PO. Also, this number is equal to the number of self-conjugated points plus the number of turning points existing on the PO.

In general, μ_t can be calculated as follows. First, the transversal monodromy matrix of the PO is computed and diagonalized. Recall that this matrix describes the linearized motion in the vicinity of a PO, and its eigenvectors, ξ_s and ξ_u, give the directions of the stable and unstable invariant manifolds in that region. A trajectory starting on the stable (unstable) manifold then approximates (separates) from the PO during the time evolution. The evolution of the eigenvectors $\xi_s(0)$ and $\xi_u(0)$ can be written, in the linear approximation, as

$$\xi_s(t) = e^{-\lambda t} F(t)\xi_s(0), \quad \xi_u(t) = e^{\lambda t} F(t)\xi_u(0),$$

where λ is the stability index of the PO. After one period of time, $\xi_s(T)$ and $\xi_u(T)$ are $e^{\lambda T}$ times shorter and larger, respectively, than the original vectors $\xi_s(0)$ and $\xi_u(0)$, the factor $e^{\lambda T}$ being equal to the absolute value of the largest monodromy matrix eigenvalue. Moreover, $\xi_s(T)$ and $\xi_u(T)$ are either parallel or antiparallel to $\xi_s(0)$ and $\xi_u(0)$, depending on whether the value of μ is either even or odd, respectively, i.e., the eigenvalues of the monodromy matrix are positive or negative. If they are positive (negative), the motion in the neighborhood of the PO is hyperbolic (hyperbolic with reflection) and $F(T)$ is equal to the unit matrix, I $(-I)$. Once the eigenvectors, $\xi_s(t)$ and $\xi_u(t)$, have been calculated, we follow the evolution of the new vectors

$$\tilde{\xi}_s(t) = e^{\lambda t}\xi_s(t), \quad \tilde{\xi}_u(t) = e^{-\lambda t}\xi_u(t),$$

which describe an unconventional motion in the vicinity of an unstable PO without hyperbolicity. For instance, let $z_{\rm PO}(t)$ be the points of the PO as a function of time. Then the evolution of a neighbor point $z(0) = z_{\rm PO}(0) + c_s\tilde{\xi}_s(0) + c_u\tilde{\xi}_u(0)$, with $|c_s|, |c_u| \ll 1$, is given by $z(t) = z_{\rm PO}(t) + c_s\tilde{\xi}_s(t) + c_u\tilde{\xi}_u(t)$. Finally, μ_t can be obtained by following the angle swept by any of the previous vectors. Let us remark that the value of μ_t is not canonically invariant, in contrast with μ.

2. The Bohr-Sommerfeld quantization rules

The smoothing process implicit in the integration on Eq. (5) renders a function with the probability density well localized along the PO. This localization effect over the PO is maximized, by constructive interference, when γ_t returns to the initial point with an accumulated phase that is a multiple of 2π. This happens when the phase fulfills the so-called BS quantization rule,

$$\frac{S_T}{\hbar} - \frac{\pi}{2}\mu = 2\pi n, \quad n = 0,1,2,\ldots. \tag{8}$$

At this point it is necessary to discuss the symmetry of the computed wave functions. The quantum eigenstates of the quartic oscillator, (1), are classified according to the C_{4v} symmetry group, which has five irreducible representations (IRs), four of which (A_1, B_1, A_2, B_2) are one-dimensional, and the other (E) two-dimensional. An elegant way to deal with this problem is to refer everything to the fundamental domain defining the potential. In our case this domain consists of the 1/8 region bounded by one semiaxis and the neighbor semidiagonal in the case of the one-dimensional representations, A and B, and the 1/4 region between the two semiaxis in the case of the two-dimensional one, E. To translate this into semiclassical arguments, the POs must be desymmetrized by "folding" the original trajectories into the fundamental domain. In this way, eigenfunction symmetry characteristics turn into boundary conditions, Dirichlet ($\psi = 0$) or Neumann ($\partial_\perp\psi = 0$), at the axis ($x, y = 0$) and the diagonals ($x = \pm y$). When dealing with POs, this is equivalent to introducing "artificial" hard walls boundaries in both the axis and the diagonals, which has two effects. First, they reduce the length and, then, the topological (without the contributions arising from the desymmetrization) and mechanical actions in Eq. (7) in an integer factor of p, given by the ratio between the period of the full PO and that of the desymmetrized PO. Second, they have an additional, more complicated effect in the Maslov index, which is different for the Dirichlet and Neumann cases, which has to be carefully taken into account. Accordingly, the quantization condition, (8), should be modified in order to quantize a desymmetrized PO of period T/p, taking into account the appropriate boundary conditions of the PO. The new BS quantization rule then reads

$$\frac{S_T/p}{\hbar} - [N_{\rm D} - N_{\rm N}]\frac{\pi}{2} - [\mu/p + N_r]\frac{\pi}{2} = 2\pi n, \tag{9}$$

where S_T/p, $\mu/p + N_r$, and N_r are, respectively, the action, winding number, and number of reflections of the desymmetrized PO. Also, the number of excitations, n, has been "reduced" to the fundamental domain. The number of Dirichlet and Neumann conditions on the wave functions at symmetry lines (axis and diagonals) are given by $N_{\rm D}$ and $N_{\rm N}$, respectively. Obviously, $N_r = N_{\rm D} + N_{\rm N}$. Furthermore, it can be shown that $\mu + 2pN_{\rm D}$ equals the Maslov index appearing in the GTF [22,36,37]. A full discussion of the derivation of Eq. (9) can be found in Ref. [23]. Finally, the semiclassically allowed BS quantized energies can be obtained by transforming Eq. (9) with the aid of scaling relation (3), thus rendering

$$\mathcal{E}_n^{3/4} = \frac{2\pi\hbar}{(S/p)}\left[n + \frac{\mu/p}{4} + \frac{N_{\rm D}}{2}\right], \tag{10}$$

where $S \equiv S_T$ is the action of the complete PO at energy $\mathcal{E} = 1$.

In Table I we summarize all the relevant dynamical information for the POs in Fig. 2 at $\mathcal{E} = 1$ [recall that they can be transformed to any other value of the energy by using the scaling relations in Eqs. (2) and (3)]. In the last column in the table, we include an adimensional parameter defined as

$$\mathcal{R} = \lambda T N_s N_t, \tag{11}$$

measuring the relative relevance of each PO, in the sense that shorter, simpler, and less unstable orbits have lower values of $\mathcal{R}$. The integers N_s and N_t take into account the spatial and

TABLE I. Classical action S, stability index λ, winding number μ, spatial and time reversal numbers N_s and N_t, and relevance $\mathcal{R}$, measured with Eq. (11), for the POs of the quartic oscillator, (1), shown in Fig. 2 at $\mathcal{E} = 1$.

PO	S	λ	μ	N_s	N_t	$\mathcal{R}$
1	22.1111	0.1014	16	2	1	3.36
2	22.0590	0.0777	14	4	1	5.16
3	8.2945	0.7669	2	2	1	9.54
4	26.0610	0.1296	14	4	1	10.12
5	10.4568	0.7120	4	1	2	11.16
6	25.0018	0.3842	12	1	2	14.40
7	9.2936	0.6032	4	4	1	16.80
8	24.9083	0.5334	8	1	2	19.93
9	21.7969	0.3197	14	4	1	20.92
10	21.3683	0.3639	12	2	2	23.33
11	20.7624	0.4291	12	2	2	26.72
12	12.7134	0.7043	4	2	2	26.88
13	14.2519	0.6469	6	4	1	27.68
14	20.0588	0.4671	10	4	2	28.12
15	19.1639	0.5070	10	4	1	29.16
16	17.0268	0.5769	8	2	2	29.48
17	15.8266	0.6237	6	4	1	29.62
18	18.2195	0.5473	8	2	2	29.92

time-reversal symmetries of the orbits: N_s corresponds to the number of different POs that are obtained by application of the C_{4v} symmetry operations, while N_t is equal to 1 when the PO is time reversal and to 2 otherwise. Note that the product $N_s N_t$ equals the number of repetitions of the PO appearing in the summation of the GTF, i.e., the number of similar POs that can be constructed at the same energy, which depends strongly on how symmetrical the PO is as well as on the IR that is being considered.

Let us consider now the effect of desymmetrization. For one-dimensional IRs, the system is desymmetrized by reducing the configuration space to the region $x \geqslant y \geqslant 0$. The corresponding desymmetrized POs are shown in Fig. 3. For the two-dimensional representation, the desymmetrized configuration space corresponds to the region $x, y \geqslant 0$, and the associated POs are plotted in Fig. 4. The corresponding information—p, N_{D}, and N_{N}—is given in Tables II and III, respectively. In Table II the reflections at the axis $x = 0$ and the diagonal $x = y$ are considered, in addition to a reflection at the y axis for orbit 1. In Table III the reflections at the x and y axis are considered. We have separated the data in E_1 and E_2 components, corresponding to the cases symmetric with respect to axis x or y and antisymmetric with respect to axis y or x, respectively. As PO numbers 2, 3, 10, 12, 14, 17, and 18 arrive at the origin $x = y = 0$ forming a nonzero angle (see Figs. 3 and 4), it is necessary in this situation to include reflections at axes x and y simultaneously.

Once the BS energies are calculated with the aid of the desymmetrized condition, (10), the corresponding tube functions over the full PO (given in Fig. 2) are computed using Eq. (5). These wave functions have n nodes in the desymmetrized region of the potential and N_{D} nodes along the symmetry lines, and they are real only if the PO shows time-reversal symmetry. If this is not the case, a real function

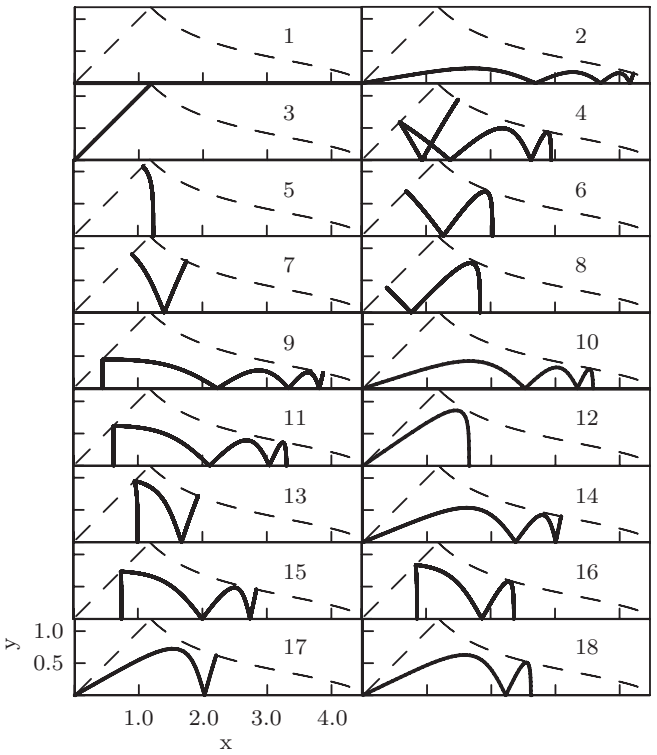

FIG. 3. Same as Fig. 2, for desymmetrized POs in the fundamental domain associated with one-dimensional irreducible representations.

can always be constructed by combination of the tube functions obtained with two Gaussian wave packets given by Eq. (6), running clock and counterclockwise along the orbit, respectively. Note, however, that the time-reversal wave functions do not

TABLE II. Period ratio p, Dirichlet number N_{D}, and Neumann number N_{N}, boundary conditions relevant for the Bohr-Sommerfeld quantization, (10), of the desymmetrized POs in Fig. 3 in the one-dimensional irreducible representations.

		A_1		A_2		B_1		B_2	
PO	p	N_{D}	N_{N}	N_{D}	N_{N}	N_{D}	N_{N}	N_{D}	N_{N}
1	2	0	1	–	–	0	1	–	–
2	2	0	8	8	0	0	8	8	0
3	2	0	2	–	–	–	–	2	0
4	2	0	9	9	0	2	7	7	2
5	4	0	2	2	0	1	1	1	1
6	4	0	4	4	0	1	3	3	1
7	2	0	3	3	0	1	2	2	1
8	4	0	4	4	0	1	3	3	1
9	2	0	9	9	0	2	7	7	2
10	2	0	7	7	0	0	7	7	0
11	2	0	8	8	0	2	6	6	2
12	2	0	3	3	0	0	3	3	0
13	2	0	5	5	0	2	3	3	2
14	2	0	6	6	0	0	6	6	0
15	2	0	7	7	0	2	5	5	2
16	2	0	6	6	0	2	4	4	2
17	2	0	4	4	0	0	4	4	0
18	2	0	5	5	0	0	5	5	0

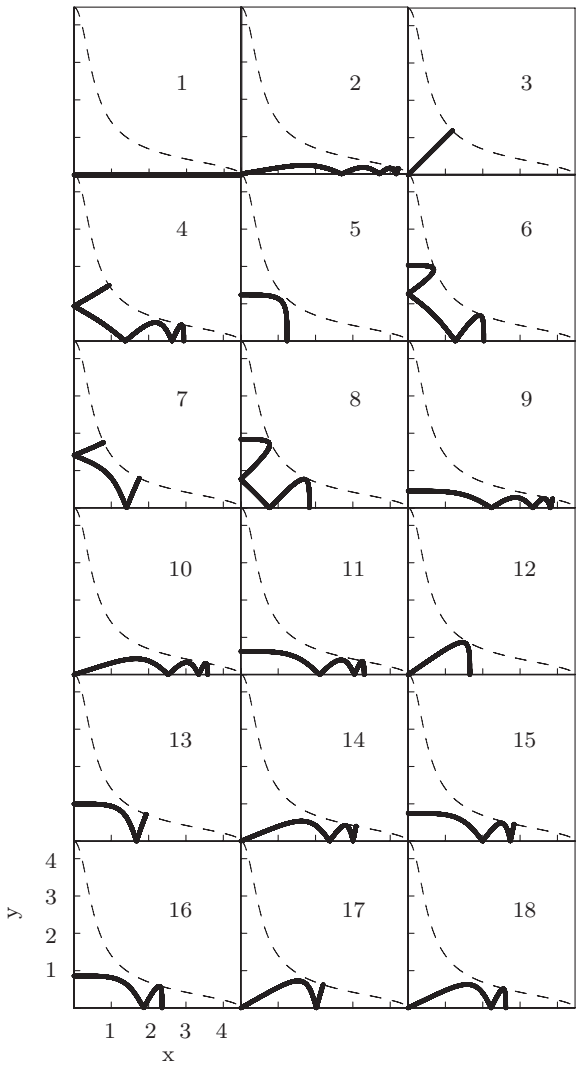

FIG. 4. Same as Fig. 3, for the two-dimensional irreducible representation, E.

belong, in general, to any of the IRs of the system. Again, this represents no problem since proper symmetry-class-adapted tube functions can be constructed combining the different wave functions obtained when the elements of the C_{4v} symmetry group act on the previously defined (real) tube functions.

TABLE III. Same as Table II, for desymmetrized POs associated with the two-dimensional irreducible representation, E, shown in Fig. 4. The data have been separated into two components, E_1 and E_2, corresponding to the cases symmetric with respect to x or y and antisymmetric with respect to y or x, respectively.

		E_1		E_2				E_1		E_2	
PO	p	N_D	N_N	N_D	N_N	PO	p	N_D	N_N	N_D	N_N
1	2	1	0	–	–	10	2	1	6	6	1
2	2	1	7	7	1	11	2	1	5	5	1
3	2	1	1	1	1	12	2	1	2	2	1
4	2	2	5	5	2	13	2	1	2	2	1
5	2	1	1	1	1	14	2	1	5	5	1
6	2	3	3	3	3	15	2	1	4	4	1
7	1	2	2	2	2	16	2	1	3	3	1
8	2	3	3	3	3	17	2	1	3	3	1
9	2	1	6	6	1	18	2	1	4	4	1

3. Computation of the scar functions

The scar functions are finally computed as an improved version of the auxiliary tube functions introduced before that includes dynamical information of the system up to Ehrenfest time, T_E. By restricting the integration time in this way, the geometrical support of the computed scar function not only is restricted to the PO itself but also includes small pieces of the associated stable and unstable manifolds attached to the PO; see, for example, the discussion in Ref. [24].

The scar functions are calculated by propagating the corresponding tube functions, (5), followed by a subsequent Fourier transform for a finite lapse of time:

$$\psi_n^{\rm scar}(x,y) = \int_{-T_E}^{T_E} dt \cos\left(\frac{\pi t}{2T_E}\right) e^{-i(\hat{\mathcal{H}}-\mathcal{E}_n)t/\hbar}\psi_n^{\rm tube}(x,y). \tag{12}$$

T_E corresponds to the lapse of time that it takes for a typical Gaussian wave packet to spread over the area, $A_{\rm tr}$, in a characteristic Poincaré SOS of the desymmetrized system, and it is related to the Lyapunov exponent, $\bar{\lambda}$, in the following way:

$$T_E = \frac{1}{2\bar{\lambda}} \ln\left(\frac{A_{\rm tr}}{\hbar}\right). \tag{13}$$

In our case $A_{\rm tr} \sim 5.5278\mathcal{E}^{3/4}$ and $A_{\rm tr} \sim 11.0555\mathcal{E}^{3/4}$ for the one-dimensional and two-dimensional IRs, respectively, and $\bar{\lambda} \sim 0.3848\mathcal{E}^{1/4}$, which does not depend on the IR since it is associated with a generic chaotic trajectory of the system.

The cosine window in expression (12) is introduced in order to minimize the energy dispersion, $\sigma = \langle\psi_n^{\rm scar}|(\hat{\mathcal{H}} - \mathcal{E}_n)^2|\psi_n^{\rm scar}\rangle$, of the scar functions [38], which can be semiclassically approximated as [27]

$$\bar{\sigma} = \frac{\pi}{2}\,\frac{\hbar\lambda(s_2+\lambda T_{\rm E})}{(s_1+\lambda T_{\rm E})(s_2+\lambda T_{\rm E})+s_2^2}, \tag{14}$$

with $s_1 \approx 1.06078$ and $s_2 = \pi/\sqrt{2} - s_1 \approx 1.16066$. Note that this magnitude depends on the IR through T_E, and then on $A_{\rm tr}$. This procedure effectively reduces the energy dispersion of the scar function with respect to the corresponding tube wave function by a factor that is proportional to $\ln(A_{\rm tr}/\hbar)$.

4. Some examples of scar functions

Let us present now some representative examples of the scar functions that are obtained for the POs in Fig. 1. The value $\hbar = 1$ is used in all quantum computations. Wavelets provide an efficient method to perform the time evolution appearing in Eq. (12), with a precision of at least six decimal places [46].

In Fig. 5 we show the probability density corresponding to the scar functions constructed over PO 5 with an excitation number $n = 2$, for all IRs in the system. Since the guiding PO does not exhibit time-reversal symmetry, time-symmetrized frozen Gaussian functions, constructed combining wave packets, (6), running clockwise and counterclockwise, have been used in the computations of Eq. (5). No additional spatial symmetrization is required in order to enforce the

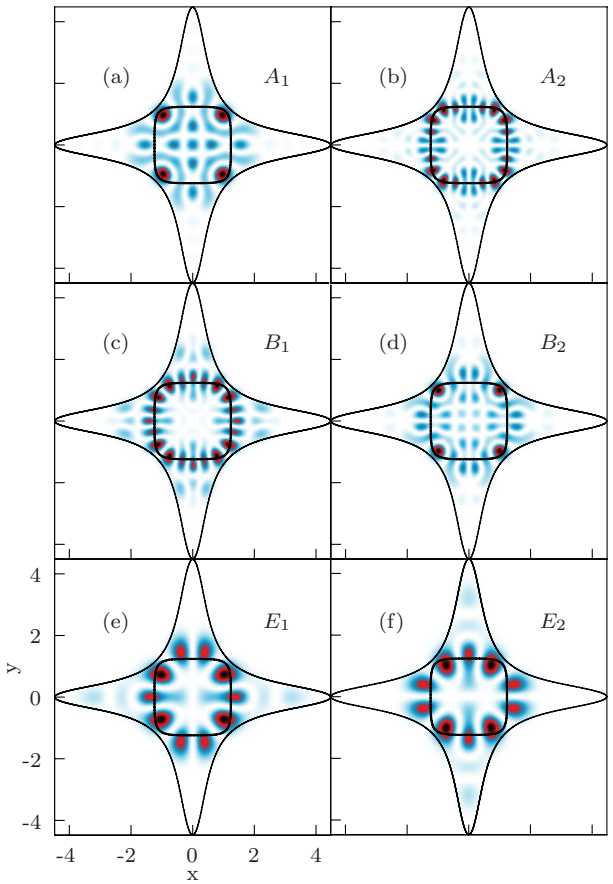

FIG. 5. (Color online) Probability density corresponding to the scar functions localized over periodic orbit 5 in Fig. 2 with $n = 2$, for the different irreducible representations in the system. The plot has been scaled to $\mathcal{E} = 1$. The scarring periodic orbit is plotted superimposed.

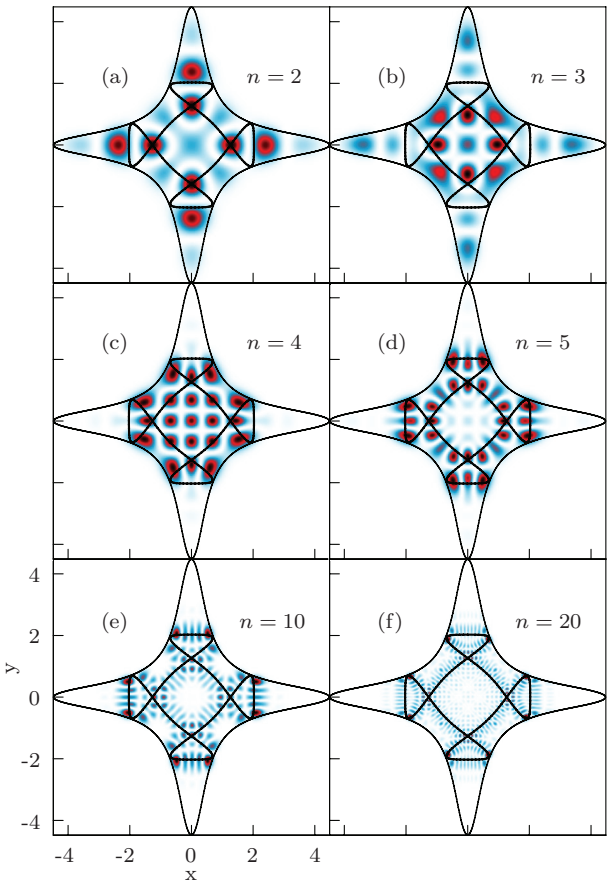

FIG. 6. (Color online) Scar wave functions with A_1 symmetry constructed using periodic orbit 6 in Fig. 2 for different values of the excitation number, n. The scarring periodic orbit is superimposed.

proper symmetry properties, since the time-symmetrized wave functions defined in this way are invariant under the action of the C_{4v} group operations. The BS quantized energies, also necessary in the calculations, were obtained with the aid of Eq. (10) using the values given in Tables I–III. As shown in Fig. 5, the number of nodes of each of the wave functions is different, and equal to $pN_t(n + N_D/2)$. Furthermore, the functions belonging to the one-dimensional IRs are either symmetric or antisymmetric with respect to both the axes and the diagonals; those belonging to the two-dimensional IR are, on the other hand, only symmetrical with respect to one axis and antisymmetrical with respect to the other. In Fig. 5(a), the A_1 scar function having 16 nodes and local maxima over the axis and the diagonals (Neumann boundary conditions) is shown. On the other extreme, the A_2 function [Fig. 5(b)] has nodes localized over these lines, exhibiting a total number of nodes of 24: 16 are "due" to the number of excitations, 4 come from the Dirichlet conditions at the axes, and the remaining 4 nodes arise from the Dirichlet conditions at the diagonals. Similarly, the B_1 (B_2) scar functions have 20 nodes over the PO, 4 of them due to the Dirichlet conditions at the diagonals (axes). Finally, for the E symmetry we have one Neumann condition over one axis and one Dirichlet condition over the other, thus producing a total number of nodes of 10.

In Fig. 6 we show the A_1 symmetry scar functions constructed using PO 6 in Fig. 2 for different values of the excitation number, n. As discussed before, these functions have been constructed imposing Neumann conditions on the boundaries of the desymmetrized POs, so that n is equal to the number of nodes in the fundamental domain, i.e., $8n$ in total. The localization on the scarred PO as n increases is notorious.

In Fig. 7 we present some results for the energy dispersion of our scar functions, together with the corresponding semiclassical estimation obtained from Eq. (14). As can be seen, our functions are very well localized in energy, and their dispersion grows moderately with it. This is a key point for the aim of this paper, since it allows the definition of a very efficient basis set.

B. Definition of the scar functions basis set: Selective Gram-Schmidt method

The second pillar of our method is the definition of the selection procedure of the scar functions forming the basis set, which is subsequently used in a standard diagonalization of the associated Hamiltonian matrix to obtain the eigenstates of the system. To define our basis set, we have generalized the usual Gram-Schmidt method (GSM) [39] and developed a new SGSM able to choose a basis set of linearly independent functions in a vectorial space from a larger (overcomplete) set

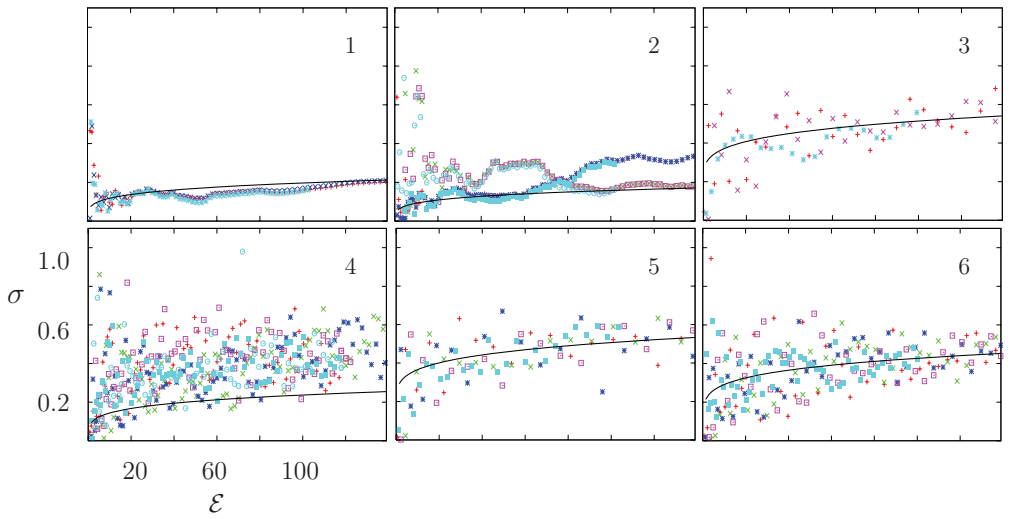

FIG. 7. (Color online) Dispersion of the scar functions of symmetry A_1 [(red) plus signs], A_2 [(green) crosses], B_1 [(dark-blue) stars], B_2 [(pink) open squares], and E [(light-blue) filled squares] constructed over periodic orbits 1–6 shown in Fig. 2. Results obtained with the semiclassical approximation, (14), are plotted superimposed on the solid black line.

of functions, which can be used to efficiently compute chaotic eigenfunctions of our system in a given energy window. The SGSM is especially useful when computing highly excited eigenfunctions in a small energy window, since the size of the basis set decreases considerably in this case. The procedure starts from an initial set of N scar functions, $|\psi_j^{(0)}\rangle$, from which the SGSM selects the minimum number of them, $N_b \leqslant N$, necessary to adequately describe the Hilbert space defined by the eigenfunctions whose energies are contained in the energy window, i.e., the SGSM defines a basis set in that window. The elements of the basis set $|\psi_{j_i}^{(0)}\rangle$, where subindex i orders the elements according to their semiclassical relevance (see discussion below), are automatically selected with the aid of the conventional GSM. Thus, associated with the basis $|\psi_{j_i}^{(0)}\rangle$, we construct an auxiliary basis $|\varphi_i\rangle$, formed by the orthogonalization of $|\psi_{j_i}^{(0)}\rangle$. For example, if we set

$$|\varphi_1\rangle = \left|\psi_{j_1}^{(0)}\right\rangle,$$

then the second auxiliary function $|\varphi_2\rangle$ is given by

$$|\varphi_2\rangle = \frac{\left|\psi_{j_2}^{(1)}\right\rangle}{\left|\psi_{j_2}^{(1)}\right|},$$

where $j_2 \neq j_1$ and

$$\left|\psi_{j_2}^{(1)}\right\rangle = \left|\psi_{j_2}^{(0)}\right\rangle - \left\langle\varphi_1\middle|\psi_{j_2}^{(0)}\right\rangle\left|\psi_{j_2}^{(0)}\right\rangle,$$

and so on.

In our SGSM method, the selection procedure of the basis functions of a given symmetry for the calculation of the eigenenergies, $\mathcal{E}$, contained in the energy window defined by

$$\mathcal{E}^- < \mathcal{E} < \mathcal{E}^+, \tag{15}$$

is done automatically by using a definite set of rules, which are based on a *semiclassical selection parameter*, η. This parameter is defined in such a way that it takes into account in a simple form the dispersion of the scar functions, the simplicity of the PO, and the density of states of the system (which is only relevant when the energy window is large). For a given scar function, η_j is given by

$$\eta_j = \rho_j\left[\sigma_j^2 + (\delta\mathcal{E}_j)^2\right]^{1/2} T_j N_{s,j} N_{t,j}, \tag{16}$$

where ρ_j is the mean density of (symmetry-class) states at the BS energy of interest ($\mathcal{E}_j$), σ_j is the dispersion of the scar function, and $\delta\mathcal{E}_j$ is defined as

$$\delta\mathcal{E}_j = \begin{cases} \mathcal{E}^- - \mathcal{E}_j & \text{if} \quad \mathcal{E}_j < \mathcal{E}^-, \\ 0 & \text{if} \quad \mathcal{E}^- < \mathcal{E}_j < \mathcal{E}^+, \\ \mathcal{E}_j - \mathcal{E}^+ & \text{if} \quad \mathcal{E}_j > \mathcal{E}^+. \end{cases} \tag{17}$$

Other criteria could be used to define the parameters introduced in Eqs. (11) and (16). For example, one could drop the function $\delta\mathcal{E}_j$ appearing in Eq. (16) and still get quite accurate results, especially in large energy windows. However, this function is included to improve the numerical accuracy by reducing the boundary effects. We thus believe that the previous equations are very straightforward in order to substitute the contribution of the longer POs appearing in the GTF by the interaction of the shortest ones, following the short PO theory developed by Vergini *et al.* [22,23,27], although other definitions are possible.

The SGSM is then defined in an algorithmic way as follows.

(0a) With the method described in Sec. III A, we compute all normalized scar functions $|\psi_j^{(0)}\rangle$ with the smallest values of $\mathcal{R}$ and BS quantized energies $\mathcal{E}_j$ in the enlarged energy window

$$\mathcal{E}^- - 2\bar{\sigma} < \mathcal{E}_j < \mathcal{E}^+ + 2\bar{\sigma}, \tag{18}$$

where $\bar{\sigma}$ is given by Eq. (14) for $\lambda \equiv \bar{\lambda}$. This is the most time-demanding step in the procedure.

It can be *a priori* expected that the overlap of the scar functions outside this enlarged window with the desired system eigenfunctions is negligible, due to the fact that they were constructed minimizing their energy dispersion.

(0b) The semiclassical selection parameter, η_j, of Eq. (16), associated with each scar function in this first approach to the final basis set, is then calculated. In this expression, ρ_j is calculated semiclassically, σ_j can be computed exactly with the aid of the wavelet basis or using Eq. (14), and the classical parameters T_j, $N_{s,j}$, and $N_{t,j}$ are calculated applying Eq. (4) to the parameters listed in Table I.

(1) From this initial set of scar functions, $|\psi_j^{(0)}\rangle$, we select a smaller number of them, $N_b \leqslant N$, forming the basis set that is optimal for our purposes, in the following way. Note that the number of scar functions calculated in this way, N, should always be greater than or equal to

$$N_b = N_{\rm sc}(\mathcal{E}^+ + 2\bar{\sigma}) - N_{\rm sc}(\mathcal{E}^- - 2\bar{\sigma}) + c_b\bar{\sigma}\rho, \tag{19}$$

where $N_{\rm sc}(\mathcal{E})$ is the semiclassical approximation to the number of states with an energy lower than $\mathcal{E}$, and the term $c_b\bar{\sigma}\rho$ enlarges the window size to take border effects into account. If this is not the case, more (longer) POs, and consequently more scar functions, must be included at this step.

The first element of our basis set is the scar function with the smallest η_j value:

$$|\varphi_1\rangle = \left|\psi_{j_1}^{(0)}\right\rangle, \quad \text{with} \quad \frac{1}{\eta_{j_1}} = \max\left\{\frac{1}{\eta_j}\right\}. \tag{20}$$

This choice gives priority to the scar functions which are more localized in energy over simpler POs, i.e., with a shorter period and being more symmetric (smaller N_{sj} and N_{tj}). In a similar way, we henceforth denote by $|\varphi_j\rangle$ the auxiliary functions necessary for the selection of the scar functions.

(2a) The remaining scar functions are then orthogonalized to function $|\psi_{j_1}^{(0)}\rangle$ using the usual GSM:

$$\left|\psi_j^{(1)}\right\rangle = \left|\psi_j^{(0)}\right\rangle - \left\langle\varphi_1\middle|\psi_j^{(0)}\right\rangle|\varphi_1\rangle, \quad j \neq j_1. \tag{21}$$

(2b) The second element of the basis set is $|\psi_{j_2}^{(0)}\rangle$, where the index j_2 satisfies $j_2 \neq j_1$, and then

$$\frac{\left|\psi_{j_2}^{(1)}\right|^2}{\eta_{j_2}} = \max\left\{\frac{\left|\psi_j^{(1)}\right|^2}{\eta_j}\right\}_{j\neq j_1}, \tag{22}$$

where the norm in the numerator has been introduced in order to make the basis-set elements as different as possible between them. Indeed, note that after the orthogonalization condition, (21), the more similar $|\psi_j^{(0)}\rangle_{j\neq j_1}$ is to $|\varphi_1\rangle$, the smaller the norm of the function $|\psi_j^{(1)}|_{j\neq j_1}$. Then the auxiliary function $|\varphi_2\rangle$ is computed as

$$|\varphi_2\rangle = \frac{\left|\psi_{j_2}^{(1)}\right\rangle}{\left|\psi_{j_2}^{(1)}\right|}. \tag{23}$$

The previous steps, 2a, and 2b, are repeated for all the remaining basis elements in the initial basis set of scar functions, in such a way that the nth step in the procedure is defined as follows.

(na) New functions are obtained by orthogonalization to the auxiliary one in the previous step, $|\varphi_{n-1}\rangle$:

$$\left|\psi_j^{(n-1)}\right\rangle = \left|\psi_j^{(n-2)}\right\rangle - \left\langle\varphi_{n-1}\middle|\psi_j^{(n-2)}\right\rangle|\varphi_{n-1}\rangle, \quad j \neq j_1, j_2, \ldots, j_{n-1}. \tag{24}$$

(nb) The nth basis element, $|\psi_{j_n}^{(0)}\rangle$, is then selected as the one for which

$$\frac{\left|\psi_{j_n}^{(n-1)}\right|^2}{\eta_{j_n}} = \max\left\{\frac{\left|\psi_j^{(n-1)}\right|^2}{\eta_j}\right\}_{j\neq j_1, j_2, \ldots, j_{n-1}}, \tag{25}$$

and then the next auxiliary function is constructed as

$$|\varphi_n\rangle = \frac{\left|\psi_{j_n}^{(n-1)}\right\rangle}{\left|\psi_{j_n}^{(n-1)}\right|}. \tag{26}$$

(nc) The procedure is finished when the number of selected elements of the basis set equals N_b given by Eq. (19).

Finally, the corresponding Hamiltonian matrix is computed in the basis set of scar functions or, alternatively, in the equivalent basis set of auxiliary functions, with the help of the wavelets, which provide an accuracy of at least 14 decimal places for the matrix elements. The diagonalization using standard routines [40] gives N_b eigenstates in the energy window defined in (15).

C. *Local* representation, scar intensities, and participation ratio

In order to analyze the performance of our method we use in this work a *local* representation, $|\varphi_j^{\rm loc}\rangle$, defined as

$$|N\rangle = \sum_j^{N_b} C_{Nj}\left|\varphi_j^{\rm loc}\right\rangle, \tag{27}$$

where the coefficients $C_{Nj} = \langle\varphi_j^{\rm loc}|N\rangle$, to reconstruct the eigenfunctions of the system in such a way that we can regain the attractive initial intuitive interpretation. Again, the procedure to compute the different $|\varphi_j^{\rm loc}\rangle$ functions is described here in an algorithmic way.

(1) The first element of the *local* representation is taken as the scar function, $|\psi_{j_1}^{(0)}\rangle$, that has the largest value of the scar intensity, x_1, defined as

$$x_j^{(n)} = \left|\left\langle\psi_j^{(n)}\middle|N\right\rangle\right|^2. \tag{28}$$

That is,

$$\left|\varphi_1^{\rm loc}\right\rangle = \left|\psi_{j_1}^{(0)}\right\rangle, \quad \text{with} \quad x_1 \equiv x_{j_1}^{(0)} = \max\left\{x_j^{(0)}\right\}. \tag{29}$$

(2a) In order to identify the second-largest scar intensity, one has to calculate the orthogonal part of the remaining scar functions, $|\psi_j^{(0)}\rangle$ to $|\varphi_1^{\rm loc}\rangle$, by computing

$$\left|\psi_j^{(1)}\right\rangle = \left|\psi_j^{(0)}\right\rangle - \left\langle\varphi_1^{\rm loc}\middle|\psi_j^{(0)}\right\rangle|\varphi_1^{\rm loc}\rangle, \quad j \neq j_1. \tag{30}$$

(2b) The second element of the *local* representation is taken as

$$\left|\varphi_2^{\rm loc}\right\rangle = \frac{\left|\psi_{j_2}^{(1)}\right\rangle}{\left|\psi_{j_2}^{(1)}\right|}, \tag{31}$$

with $x_2 \equiv x_{j_2}^{(1)} = \max\{x_j^{(1)}, j \neq j_1\}$.

The procedure is then continued, so that the nth element of the *local* representation is computed in a similar way.

(na) The orthogonal part of the functions $|\psi_j^{(n-2)}\rangle_{j\neq j_1, j_2, \ldots, j_{n-1}}$ to $|\varphi_{n-1}^{\rm loc}\rangle$ is calculated by computing

$$\left|\psi_j^{(n-1)}\right\rangle = \left|\psi_j^{(n-2)}\right\rangle - \left\langle\varphi_{n-1}^{\rm loc}\middle|\psi_j^{(n-2)}\right\rangle|\varphi_{n-1}^{\rm loc}\rangle. \tag{32}$$

(nb) Then the nth element of the *local* representation is given by

$$\left|\varphi_n^{\rm loc}\right\rangle = \frac{\left|\psi_{j_n}^{(n-1)}\right\rangle}{\left|\psi_{j_n}^{(n-1)}\right|}, \tag{33}$$

with $x_n \equiv x_{j_n}^{(n-1)} = \max\{x_j^{(n-1)}, j \neq j_1, j_2, \ldots, j_n\}$.

Let us remark here that the scar intensities, x_j, provide information on the localization properties of the eigenfunctions. However, although the largest scar intensity, x_1, provides reliable information on the localization on $|\psi_{j_1}^{(0)}\rangle$, the same is not true of $|\psi_{j_n}^{(0)}\rangle$ since, in their construction, the contribution in the subspace that spanned the functions defined previously in the SGSM was subtracted. Nevertheless, the sum $x_1 + x_2 + \cdots + x_n$ provides information on the projection of $|N\rangle$ onto the subspace defined by $|\psi_{j_1}^{(0)}\rangle, |\psi_{j_2}^{(0)}\rangle, \ldots, |\psi_{j_n}^{(0)}\rangle$.

Let us finally present some useful results concerning the scar intensities defined in Eq. (28). Assuming that the distribution of these magnitudes follows a Gaussian law for chaotic eigenfunctions, a semiclassical approximation for the average can be obtained, as discussed in Ref. [41]. Indeed, the averaged value of the jth largest scar intensity is given by

$$\bar{x}_j \simeq \frac{1}{\bar{\sigma}_r}\left(\frac{2}{\pi}\right)^{1/2}\left[\alpha_j - \ln\left(\alpha_j + \frac{9}{8}\right) + b_j + \frac{b_j^2}{2}\right], \tag{34}$$

where

$$\bar{\sigma}_r = \rho\sigma_N, \quad \alpha_j \equiv \bar{z}_j + \ln\frac{\sqrt{2}\bar{\sigma}_r}{j}, \quad b_j \equiv \frac{\ln(\alpha_j + 287/128)}{\alpha_j + 17/8}, \tag{35}$$

z being a random variable with averages $\bar{z}_1 \simeq 0.577$ and $\bar{z}_2 \simeq 13/48$ for the two largest scar intensities. Let us remark that $\bar{x}_j$ goes, respectively, to 0 and ∞ for large and low values of the energy. Also, the above-defined semiclassical expression can be improved by including a higher order correction term in α_j, so that $\alpha_j \equiv \bar{z}_j + \ln(\sqrt{2}\bar{\sigma}_r/j + c_j)$. Adequate values for c_j are obtained by fitting to actual quantum calculations of x_j. Note that these corrections are of order $\mathcal{O}(1/\bar{\sigma}_r)$, while $\alpha_j = \mathcal{O}(1/\ln\bar{\sigma}_r)$.

We conclude this subsection by considering the participation ratio, R, that is defined, taking into account expression (27), as

$$R = \frac{\sum_{j=1}^{N_b} C_{Nj}^2}{\sum_{j=1}^{N_b} C_{Nj}^4}. \tag{36}$$

This magnitude gives us an idea of the number of basis elements that are approximately necessary to reconstruct the original eigenstate, $|N\rangle$. Accordingly, this is a parameter very relevant for our discussions, since it can be used to compare the quality of two different basis sets. Namely, the lower the value of the R, the better the basis.

IV. RESULTS

In this section we present and analyze our results on the use of scar functions as basis sets for the calculation of eigenstates of classically chaotic systems.

A. Calculation of the eigenstates

The lowest eigenvalues and eigenfunctions of the Hamiltonian operator corresponding to the quartic oscillator defined in Eq. (1) have been calculated using a basis set of scar functions constructed using the SGSM defined above. For this purpose, the 18 POs presented in Fig. 2, chosen using the relevance parameter defined by Eq. (11), have been used. From them, an initial basis set of scar functions was constructed, defined by the reference energies $\mathcal{E}^- = 0$ and $\mathcal{E}^+ = 135$, 150, 140, 140, and 82, with $\bar{\sigma} = 0.5433$, 0.5526, 0.5465, 0.5465, and 0.4622, for the symmetry classes A_1, A_2, B_1, B_2, and E, respectively. This initial basis set consists of ∼900 scar functions for each of the one-dimensional symmetry classes—A_1, A_2, B_1, and B_2—and also for E_1 and E_2. The associated energies were obtained from the BS quantization rule, (10), using the parameters given in Tables I–III. The lowest values corresponding to the A_1 symmetry class, rescaled with a power of 3/4 so that they appear equally spaced, are represented by thin black lines in Fig. 8. The next step in our procedure is the reduction of this initial basis set. This is done by applying the SGSM described in Sec. III B, using a value of $c_b = 2$ in Eq. (19). With this criterion, ∼420 scar functions of each one-dimensional and E_1 and E_2 symmetry classes are automatically selected, out of the whole set. The energies corresponding to these selected A_1 scar functions are highlighted as thick (blue) bars in Fig. 8.

Using the resulting final basis set, we have computed the corresponding Hamiltonian matrix and, by direct diagonalization, the eigenenergies and eigenfunctions of the system. The results for the 270 low-lying states of A_1 symmetry are shown in the leftmost (red lines) column in Fig. 8. In Table IV the 50 low-lying numerical values for all symmetries are reported.

Several comments are in order. First, a careful comparison reveals that the first ∼400 of each symmetry have the same accuracy (not only the eigenenergies but also the eigenfunctions) that is obtained with other standard methods [1], and thus the number of well-converged states in our calculation is of the same order as the number of elements in the basis set. Second, some first qualitative conclusions regarding the excellent performance of our basis set can be obtained from a careful consideration of the results presented in Fig. 8. To this end, recall again the extremely low dispersion of our scar functions, which means that they minimally spread among (or contribute to) states in the eigenenergy spectrum far from their BS quantized energies. For example, for the most excited states only ∼6 scar basis functions are needed for a satisfactory description. This number decreases dramatically for smaller excitations, reaching as low as ∼1 for states in the interval $\Delta\mathcal{E} \sim$ 0–5, ∼2 for states in the interval $\Delta\mathcal{E} \sim$ 5–10, and so on, as the scar states get "bright," being highlighted as thick (blue) bars in Fig. 8. This argument is made more quantitative in the rest of the discussion presented in this section, particularly when the eigenstate participation ratios are considered. Finally, it is worth emphasizing that, besides the type of calculation presented here, namely, the computation of the low-lying eigenstates, the SGSM introduced in this work can be advantageously used in the computation of eigenstates in an energy window, i.e., $\mathcal{E}^- \neq 0$, something which is especially useful to compute only highly excited eigenfunctions with small basis sets. This is something that we have tested for different energy ranges. In the next subsection

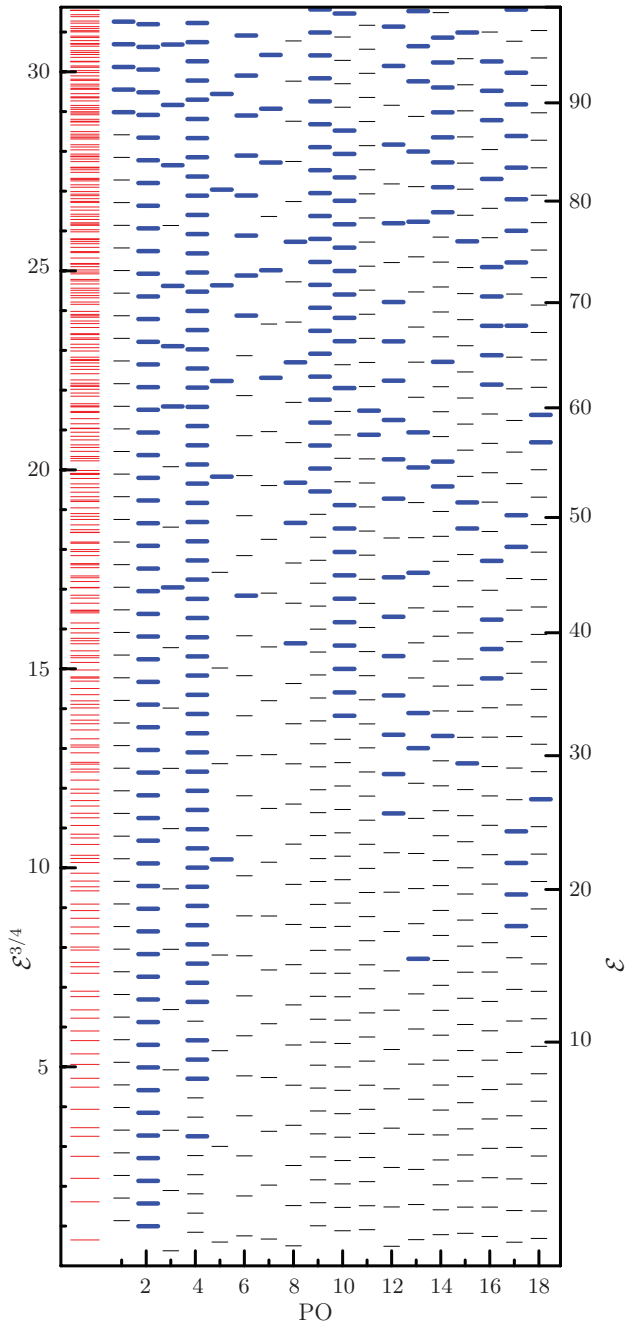

FIG. 8. (Color online) Scaled energies for the A_1 states of the quartic oscillator, (1): leftmost (red) column, numerical eigenenergies; thin (black) lines, BS quantized energies; thick (blue) bars, energies of the scar functions selected by the SGSM.

we present the results associated with the eigenfunctions $|N\rangle_{A_1}$ with $N = 271$–282, calculated restricting the calculation to the energy window $100 < \mathcal{E} < 103$ with a basis set formed by only 25 scar functions. It is quite impressive that, using such a small basis set, the error in the energy is lower than 0.12 in units of the mean level spacing (actually, it is even lower than 0.06 for all the computed eigenvalues except for $|279\rangle_{A_1}$), whereas the overlap of all the computed eigenfunctions with the corresponding exact ones exceeds 99.8%. Further details on these results are presented in the following section.

TABLE IV. Eigenenergies, $\mathcal{E}$, for the eigenstates of the quartic oscillator, (1), obtained with our basis set of scar functions.

N	A_1	A_2	B_1	B_2	E
1	0.56323	4.1023	1.6175	2.5230	1.2241
2	1.8848	5.9503	2.7455	4.7256	2.2570
3	2.8638	7.5442	3.8675	6.0561	3.2537
4	3.8563	8.9638	5.0139	7.2567	3.6376
5	4.8286	9.7951	6.1773	8.2227	4.4506
6	5.2584	10.658	6.8364	9.1029	5.1299
7	6.2126	11.985	7.4816	10.468	5.5775
8	7.4115	12.861	8.7094	11.352	6.2642
9	7.9052	13.616	9.3168	11.914	6.8080
10	8.6947	14.793	10.080	12.708	6.9510
11	9.3055	15.393	11.188	13.637	7.9451
12	10.087	16.069	11.534	14.276	8.1741
13	10.664	16.731	12.525	15.134	8.3392
14	11.452	17.702	12.908	15.928	9.3842
15	11.960	18.287	13.550	16.571	9.4158
16	12.790	19.115	14.309	17.215	9.8674
17	13.140	20.011	14.934	18.242	10.448
18	14.298	20.467	15.827	18.702	10.804
19	14.714	21.183	16.234	18.976	11.013
20	15.003	21.789	17.007	19.988	11.520
21	15.831	22.345	17.391	20.220	12.004
22	16.024	23.217	18.099	21.270	12.267
23	16.924	23.673	18.928	21.821	12.786
24	17.384	24.062	19.068	22.073	13.091
25	17.989	24.810	19.885	23.038	13.526
26	18.517	25.348	20.202	23.556	13.814
27	18.972	26.495	20.604	24.428	14.109
28	19.905	26.629	21.668	24.591	14.541
29	20.184	27.083	22.118	25.140	14.729
30	20.592	27.860	22.358	25.967	15.069
31	21.163	28.462	23.087	26.104	15.646
32	21.931	28.946	23.754	26.682	15.893
33	22.228	29.614	24.066	27.357	16.209
34	22.458	29.711	24.939	27.950	16.600
35	23.247	30.334	25.079	28.478	16.801
36	23.727	31.099	25.513	29.093	17.373
37	24.010	31.516	25.916	29.241	17.407
38	24.653	32.199	26.817	30.233	17.768
39	25.231	32.626	27.121	30.333	18.152
40	25.576	32.831	27.443	31.015	18.339
41	26.121	33.681	28.180	31.511	18.764
42	26.530	34.089	28.491	32.184	19.147
43	27.098	34.516	28.932	32.312	19.174
44	27.403	35.335	29.345	33.214	19.765
45	28.097	35.928	29.980	33.441	20.005
46	28.727	36.002	30.711	34.020	20.136
47	28.946	36.551	31.076	34.323	20.642
48	29.342	36.933	31.467	34.651	20.898
49	29.475	37.373	31.568	34.953	21.120
50	30.225	37.855	32.483	35.880	21.440

B. Reconstruction of the eigenfunctions

Let us now analyze the results obtained in the previous subsection. First, we discuss the structure of some representative examples of the eigenfunctions obtained for the quartic oscillator, (1), with our basis set of scar functions, by

examining their reconstruction using the *local* representation described in Sec. III C.

We start with the simplest case, which corresponds to states with eigenfunctions that appear strongly scarred in the sense discussed by Heller in Ref. [6]. This happens, for example, for states $|208\rangle_{A_1}$, $|291\rangle_{A_1}$, and $|303\rangle_{A_1}$, which are highly localized over POs 3, 8, and 1 in Fig. 2, respectively. The probability densities are shown in Figs. 9(d)–9(f). In all cases, the first, and almost exclusively contributing, element of the reconstruction is a scar function corresponding to the PO scarring the eigenfunction, as would be expected *a priori*. These scar functions, which are labeled $|\mathrm{PO},n\rangle_\chi$—with PO indicating the number of the orbit in Fig. 2, n the number of excitations along it corresponding to the BS quantization condition, (10), and χ the IR—are presented in Figs. 9(a)–9(c). The PO has been plotted superimposed on the corresponding probability density. The associated energies are given in the lower-left corner of each panel. In the lower-right corner of Figs. 9(a)–9(c), we have indicated the value of the overlap between the eigenstate and the basis-set scar function. As can be seen, this overlap is always larger than 86.0% in all cases considered here. Furthermore, the fact that these states are well

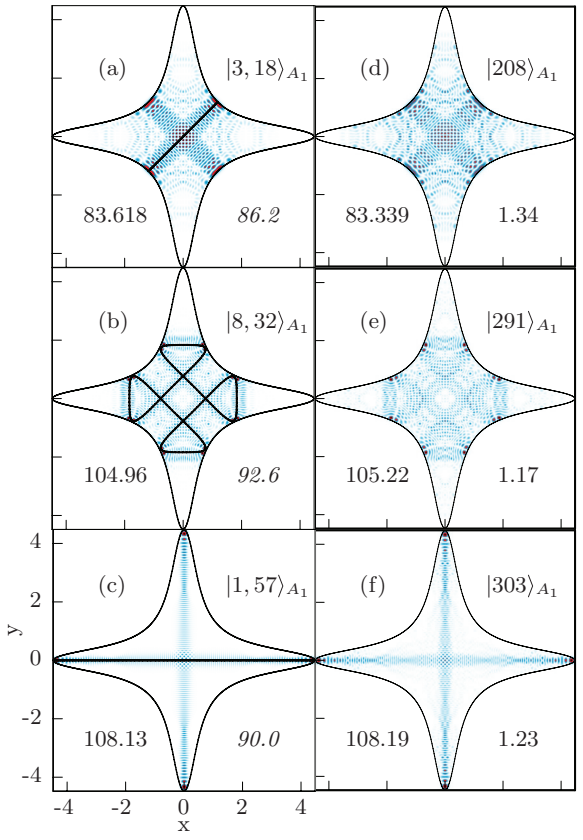

FIG. 9. (Color online) (d)–(f) Probability density for the eigenfunctions $|208\rangle_{A_1}$, $|291\rangle_{A_1}$, and $|303\rangle_{A_1}$ obtained from our variational calculation using a basis set of scar functions. (a)–(c) The same functions reconstructed using only one scar function $|\mathrm{PO},n\rangle_{A_1}$ of the basis with the corresponding scarring periodic orbit superimposed. The energy is shown in the left corner of each panel, and the overlaps of the eigenfunctions with the scar functions and the participation ratios are given in the right corners of the panels (a)–(c) and (d)–(f), respectively.

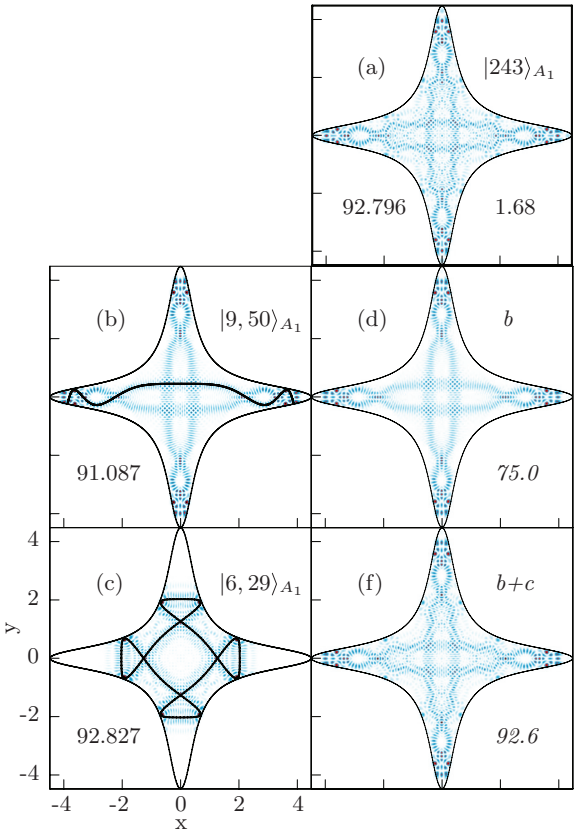

FIG. 10. (Color online) Same as Fig. 9, for the eigenfunction $|243\rangle_{A_1}$ (a), which requires two scar functions, $|9,50\rangle_{A_1}$ (b) and $|6,29\rangle_{A_1}$ (c), for its reconstruction, which is shown in (d) and (e). The information included in each panel is the same as in Fig. 9.

represented by only one state in the scar basis set makes the values of the corresponding participation ratio very low, as discussed in Sec. IV D. The values of these participation ratios are given in the right corners of Figs. 9(d)–9(f).

Let us next consider eigenstates with a more complex structure. This is the case, for example, of $|243\rangle_{A_1}$ shown in Fig. 10(a). As can be seen in Fig. 10(a), the eigenfunction for this state is concentrated on a single PO, i.e., PO 9, but the localization is not as strong as in the previous examples. Actually, the reconstruction of this eigenstate requires the combination of at least two scar functions, as the results presented in the other panels indicate. Indeed, the scar basis function $|9,50\rangle_{A_1}$, shown in Fig. 10(b), only accounts for 75.0% of the eigenstate, while when function $|6,29\rangle_{A_1}$ [cf. Fig. 10(c)] is included, this figure increases to an acceptable 92.6%. As discussed before, the corresponding value of the participation ratio is expected to be larger, $R = 1.68$, in this case.

A similar example, but with an eigenfunction exhibiting an even more complicated structure is shown in Fig. 11. In this case, the eigenfunction $|201\rangle_{A_1}$, which is localized over the "box" PO 5 [see Fig. 11(a)], requires the combination of at least four scar functions localized over different POs [see Figs. 11(b)–11(e)] for an adequate reconstruction. The relevant figures for this reconstruction, i.e., overlaps and participation ratios, are indicated in the figure, and the same comments made before apply to this case.

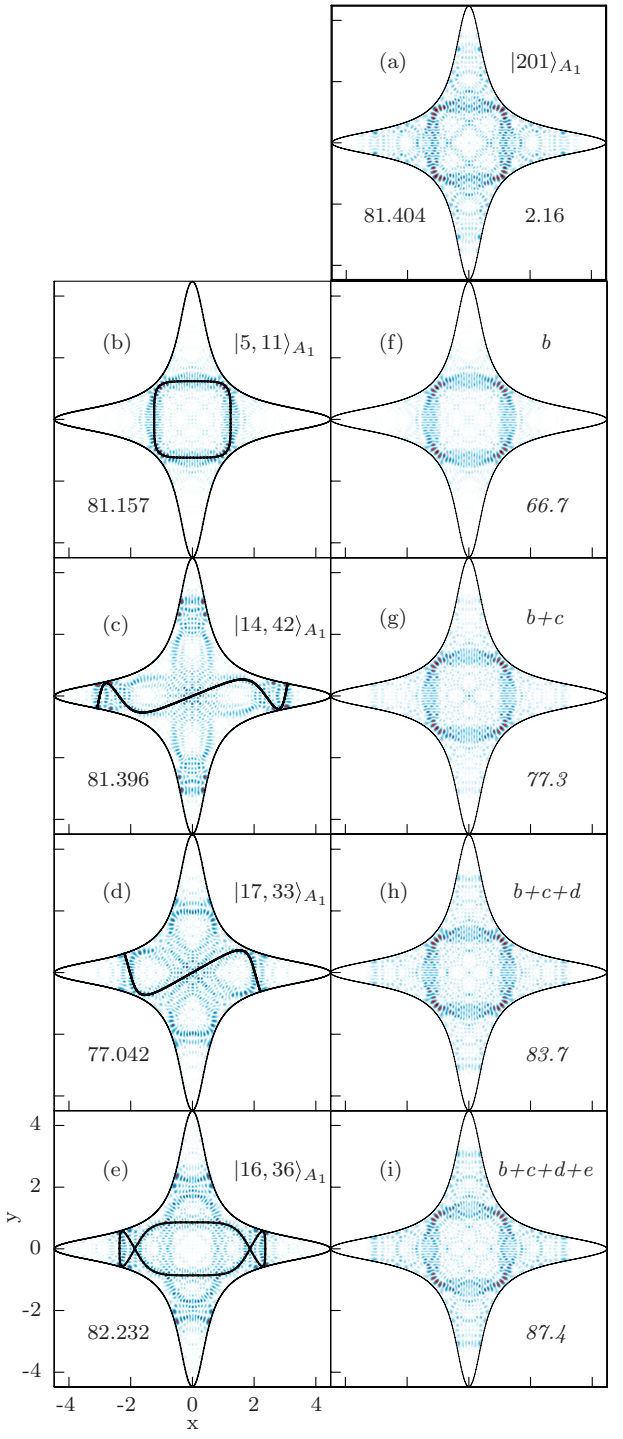

FIG. 11. (Color online) Same as Fig. 10, for $|201\rangle_{A_1}$, which requires four scar functions for its reconstruction.

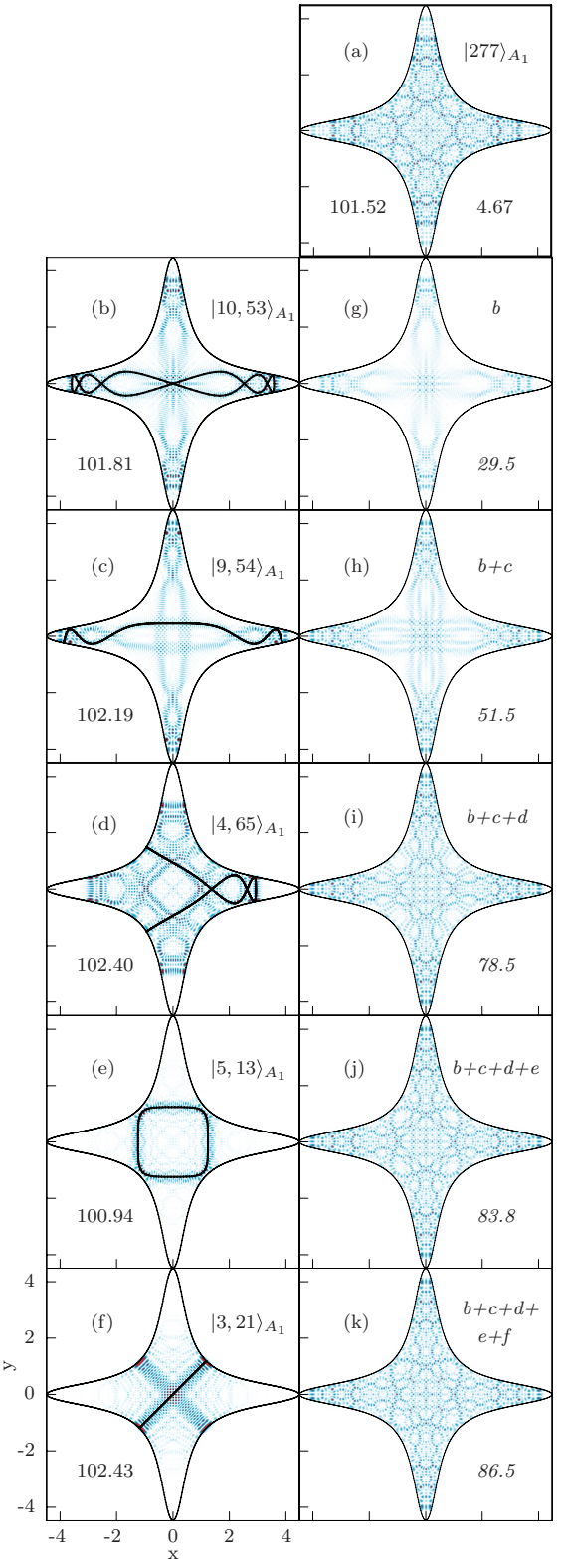

FIG. 12. (Color online) Same as Fig. 10, for $|277\rangle_{A_1}$.

To conclude this series of examples, let us consider, finally, the most general case, consisting of (nonscarred) eigenstates showing the very irregular patterns characteristic of chaotic states [42]. For this purpose, we present in Figs. 12(a) and 13(a) the probability density for states $|277\rangle_{A_1}$ and $|327\rangle_{A_1}$, respectively. The complex nodal structure inherent to these wave functions can be unfolded, however, by our SGSM, which reveals the importance of each PO, thus proving a dynamically oriented analysis of them. As can be seen, the two cases considered here are essentially reconstructed by combining only five scar functions, which are also shown in order of importance in Figs. 12(b)–12(f) and 13(b)–13(f).

From the data contained in the figures, note how, in all the examples presented here, the scar functions giving the largest

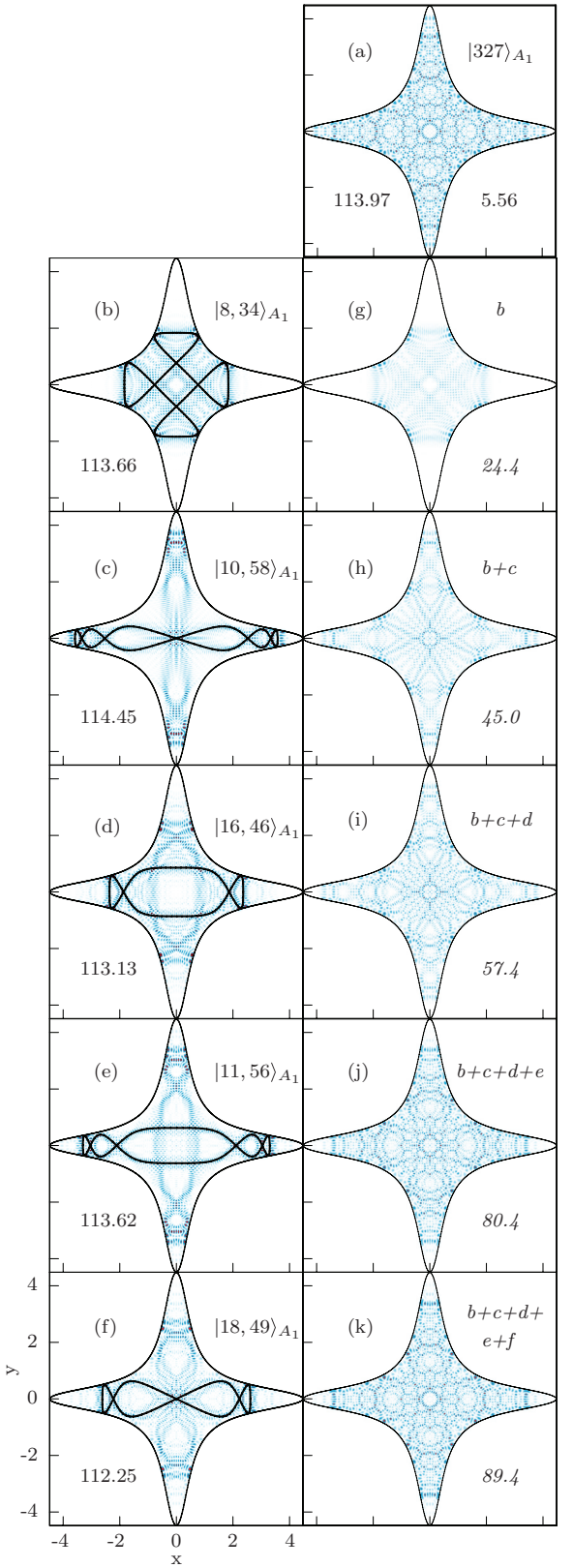

FIG. 13. (Color online) Same as Fig. 10, for $|327\rangle_{A_1}$.

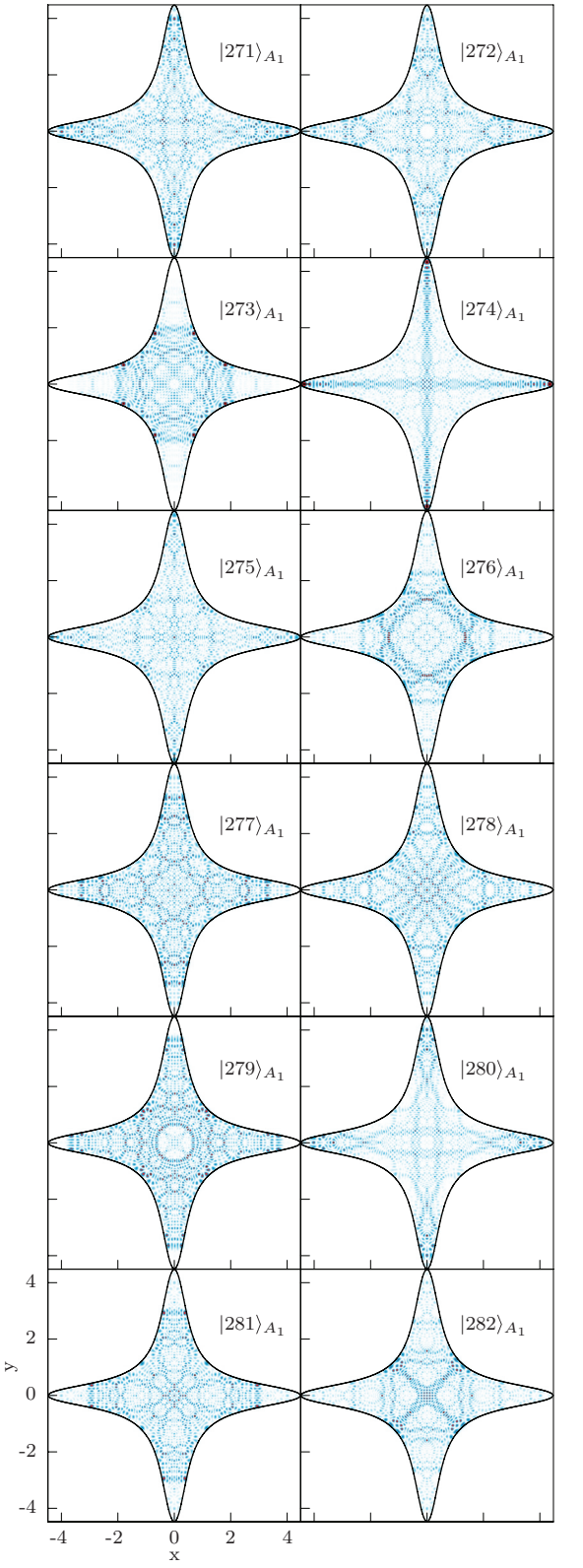

FIG. 14. (Color online) Quartic oscillator eigenfunctions $|N\rangle_{A_1}$ corresponding to the reconstruction data in Table V. Same coordinates and scaling as in Fig. 5.

contributions to the reconstruction of a given eigenstate are those whose BS quantized energies are closer to that of the corresponding eigenenergy.

We close this subsection by presenting in Table V the structure of the eigenfunctions calculated in the energy window $100 < \mathcal{E} < 103$. These eigenfunctions are shown in Fig. 14.

TABLE V. Reconstruction of the eigenstates $|N\rangle_{A_1}$ calculated in the energy window $100 < \mathcal{E} < 103$ with the 25 scar functions $|\mathrm{PO},n\rangle_{A_1}$. The participation ratio, R, defined in Eq. (36) and the accumulated reconstruction overlap, $\Sigma\%$, are also listed.

N	R	PO,n,$\Sigma\%$									
271	4.81	9,53,40.5	9,53,40.5	4,64,56.8	8,31,62.6	18,45,69.5	14,49,74.0	15,47,77.9	5,13,81.4	10,52,84.5	17,39,87.4
272	3.53	15,47,48.4	13,35,62.2	9,53,76.7	10,52,82.4	4,64,86.5					
273	2.09	8,31,67.6	6,31,76.6	5,13,87.1							
274	2.00	1,54,69.7	5,13,78.2	8,31,84.0	18,45,88.1						
275	5.24	2,54,31.0	5,13,55.9	8,31,69.0	13,35,76.0	4,64,84.9	17,39,87.5				
276	3.36	6,31,28.7	8,31,72.6	10,53,85.5							
277	4.68	10,53,29.5	9,54,51.5	4,65,78.5	5,13,83.8	3,21,86.5					
278	5.27	10,53,30.8	3,21,53.3	4,65,71.4	17,40,78.2	18,46,82.0	6,31,84.6	8,31,86.3			
279	7.85	9,54,21.8	4,65,34.2	15,48,40.1	3,21,45.5	13,36,52.5	5,13,56.1	2,55,58.5	1,55,79.4	1,54,81.1	17,40,81.9
		18,46,88.1									
280	2.08	9,54,67.7	15,48,71.3	16,43,73.9	10,53,76.5	5,13,77.5	18,46,78.3	13,36,79.2	2,55,79.9	1,55,92.6	
281	3.30	17,40,49.3	15,48,69.7	9,54,77.9	4,65,85.4						
282	4.20	3,21,44.3	13,36,52.7	15,48,65.7	11,52,73.7	4,65,82.0	10,53,84.1	9,54,86.1			

As in the previous examples, most of the probability density is reconstructed by combining few basis elements, thus demonstrating the efficiency of our method for the calculation of excited states.

Further results on the structure of the eigenfunctions of the quartic oscillator in our scar function basis set are systematically presented in the Supplemental Material [43].

C. Scar intensities

A more global idea of how the eigenfunctions are reconstructed by the scar functions can be obtained by considering the corresponding scar intensities defined in Eq. (28). In the two panels in Fig. 15 we show [(pink) plus signs] the variation with the energy of the two largest scar intensities, x_1 and x_2, for the computed A_1 eigenfunctions. Recall that these quantities give the (squared) contribution of the two most important scar functions in the *local* representation of each eigenfunction. As can be seen, both x_1 and x_2 fluctuate violently, thus appearing rather dispersed in the figure. To clearly observe the tendency in the data we have also plotted the corresponding mobile mean [(blue) crosses], computed using 20 points. The results indicate that the largest intensity, x_1, starts from a very high value and then monotonically decreases, first very rapidly up to $\mathcal{E} \sim 22$, and then much more slowly, never getting below a mean of $\sim$0.4 in the energy range that we are considering. Note that the points where x_1 is much larger that its average value correspond to scarred states in the sense of Heller [6]. Simultaneously, the second-largest contribution, x_2, first increases up to $\sim$0.2 at $\mathcal{E} \sim 22$ and then decreases extremely slowly (note that although this behavior in not noticeable in the plot, this is true since $x_1 > x_2$). Moreover, the values given by the semiclassical approximations, (34), without and with the higher order correction terms with $c_1 \simeq -c_2 \simeq 0.30$, have also been plotted, superimposed, by solid (red) and dashed (green) lines, respectively. The agreement between the quantum and the semiclassical calculations, particularly in the second case [dashed (green) line], is rather good, except for low values of the energy due to the (unrealistic) singularity inherent in Eq. (34).

Similar results for the A_2 eigenstates are shown in Fig. 16. Here, only the values of the averages and the semiclassical estimates are shown, for simplicity. The same comments made before, for the A_1 symmetry, apply.

D. Participation ratios

Also interesting for the analysis of the eigenstate structure is the consideration of the participation ratios discussed in Sec. III C. To give an idea of the expected bounds for these

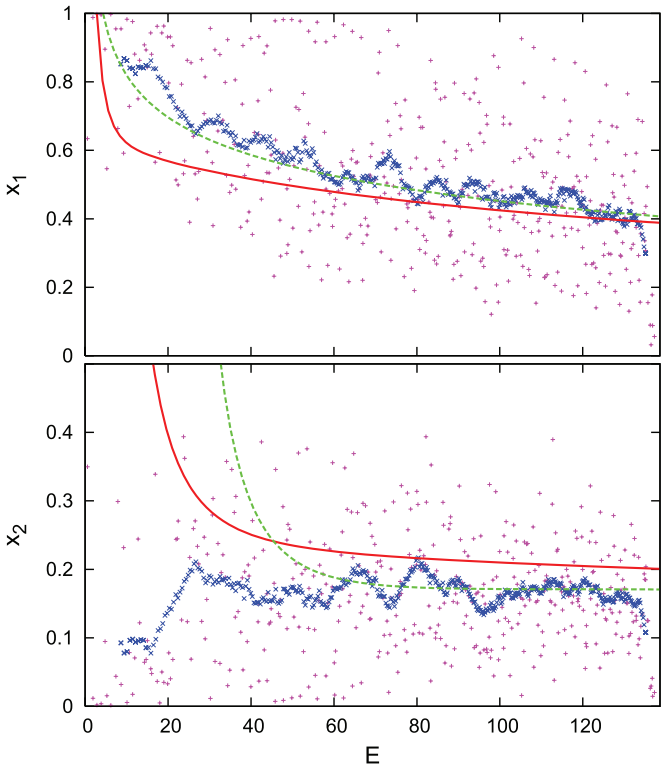

FIG. 15. (Color online) Largest scar intensities x_1 (top) and x_2 (bottom) [(pink) plus signs] for the eigenfunctions with A_1 symmetry obtained in our calculation with a basis set of scar functions. The average value, computed as a mobile mean, is plotted superimposed with (blue) crosses. The semiclassical estimates obtained with Eq. (34) for $c_1 = c_2 = 0$ and $c_1 \simeq -c_2 \simeq 0.30$ are also plotted, with solid (red) and dashed (green) lines, respectively.

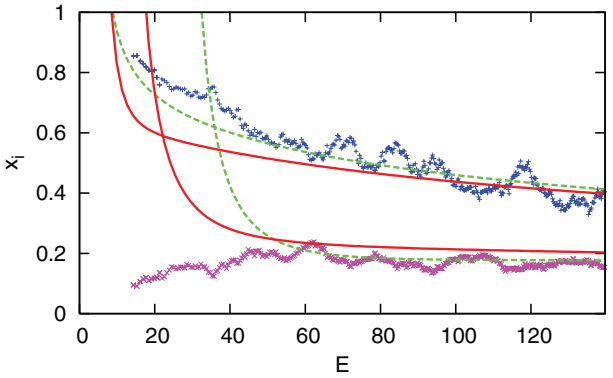

FIG. 16. (Color online) Average value of the largest scar intensities x_1 [upper (blue) plus signs] and x_2 [lower (pink) crosses] of the eigenfunctions of A_2 symmetry. The semiclassical estimates obtained with Eq. (34) are also plotted, by solid (red) and dashed (green) lines, respectively.

variables let us consider two extreme cases. First, the minimum value of the participation ratio is equal to $R_{\min} = 1$, which is obviously obtained when the system eigenfunctions are used. On the other extreme, a large value of the participation ratio corresponds to a situation where all basis functions contribute significantly to the description of each eigenstate. One such case, which, however, retains the character and thus the efficiency of a semiclassical description, is that in Ref. [4]. There, all calculations are done in a characteristic Poincaré SOS of an ergodic system. Accordingly, (i) the size of the basis set, N_b, can be estimated by the Weyl expression $N_b = A_{tr}/(2\pi\hbar)$, $A_{\rm tr}$ being the area in the SOS, and (ii) all the coefficients in a normalized expansion are expected to behave as random complex independent variables following a Gaussian distribution of zero mean and dispersion $1/N_b^{1/2}$. Thus, it is straightforward to show that

$$R_{\rm sc} = \frac{A_{\rm tr}}{4\pi\hbar}. \tag{37}$$

Let us remark that $R_{\rm sc}$ is still a reasonably small value, since it is associated with an optimized, in the semiclassical sense, basis set, thus giving participation ratio values much lower than, for example, for other frequently used basis sets, such as harmonic oscillator products [1] or a discrete variable representation [44].

In Fig. 17 we plot with (pink) plus signs these participation ratios in the *local* representation as a function of the energy for the A_1 (top) and the A_2 (bottom) symmetry eigenfunctions, respectively. Similarly to what happens with the scar intensities we find a wildly oscillatory behavior. Accordingly, we consider the averaged value, computed again as a mobile mean, which is also shown in the graph using (blue) crosses. The results obtained with the semiclassical expression, (37), have also been plotted for comparison by the dashed (green) line. As can be seen, for energies up to $\mathcal{E} \sim 22$ the values of the participation ratios are very low, always lower than 3. As the energy increases the mean participation ratio also increases, but very moderately, and it can be accurately fitted with the simple expression [also shown in Fig. 17, by the

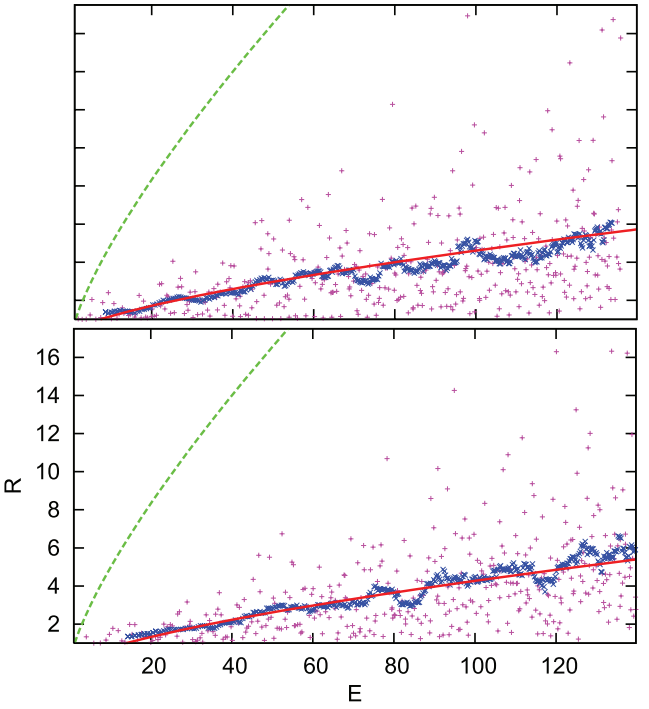

FIG. 17. (Color online) Participation ratio in the basis set of scar functions (pink crosses) for the eigenfunctions of A_1 (top) and A_2 symmetry, as a function of the energy. The average, computed as a mobile mean, is shown by blue crosses, and it is well approximated by the solid (red) curve given by the simple expression, (38). The dashed (green) line represents the semiclassical estimate given by Eq. (37).

solid (red) line]

$$\bar{R} = \zeta\bar{\sigma}_r, \tag{38}$$

in terms of the variable $\bar{\sigma}_r$ defined in Eq. (35). Here $\zeta = 8/3$ for the one-dimensional symmetry representations, A and B, and $\zeta = 2$ for the two-dimensional one, E. The moderate increment behavior found is an indication of the quality and good performance of the scar basis set we have used in our calculation and shows how a given eigenstate can be reconstructed with just a few basis functions. Actually, it has been numerically checked that for the cases with the highest values of the participation ratio, this number can be substantially reduced by increasing the size of the basis by including more POs.

The participation ratio results can be further analyzed by considering the associated statistics. For this purpose we define the adimensional coefficient

$$r = \frac{R-1}{\bar{R}}, \tag{39}$$

which is a positive random variable that is found to follow the Weibull distribution [45],

$$P_{\rm W}(x) = \frac{k}{l}\left(\frac{x}{l}\right)^{k-1} e^{-(x/l)^k}, \tag{40}$$

k and l being fitting parameters. The associated accumulated distribution can be easily calculated as

$$W_{\rm W}(r) = \int_0^r P_{\rm W}(x)\,dx = 1 - e^{-(r/l)^k}. \tag{41}$$

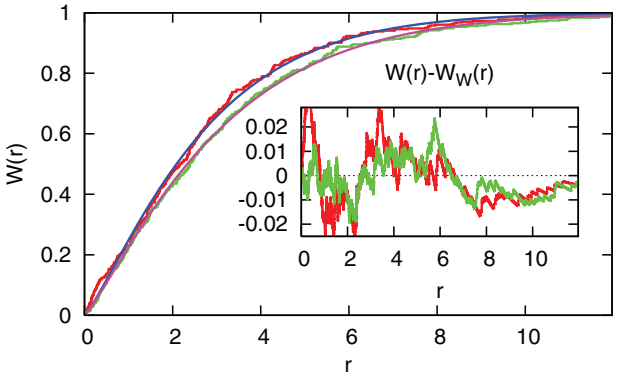

FIG. 18. (Color online) Accumulated probability distribution, $W(r)$, of the participation ratio adimensional coefficient, r, for the eigenfunctions of A_1 [upper (red) points] and A_2 [lower (green) points] symmetry obtained in our calculation with a basis set of scar functions. The corresponding values of the Weibull distribution, $W_{\rm W}(r)$, for $l_{A_1} = 2.8323 \pm 0.0003$, $k_{A_1} = 1.2030 \pm 0.0002$, $l_{A_2} = 3.1867 \pm 0.0001$, and $k_{A_2} = 1.1753 \pm 0.0001$ are shown by the solid (blue) and dashed (pink) lines, respectively. Inset: The difference $W(r) - W_{\rm W}(r)$.

The corresponding results for both the computed and the fitted accumulated distributions $W(r)$ and $W_{\rm W}(r)$ for the eigenfunctions of A_1 and A_2 symmetry are shown in Fig. 18. The difference between $W(r)$ and $W_{\rm W}(r)$, or error, is also shown in the inset. As can be seen, this difference is very small for both symmetries, as is also the case for the rest of the symmetry classes.

E. Upper bounds to errors in eigenenergies and eigenfunctions

In this subsection we obtain expressions for the upper bound to the error in the eigenenergy and eigenfunctions obtained in our calculation versus their dispersion [27]. These upper bounds are specially useful in the calculation of highly excited states, when large basis sets are required.

Usually, the convergence of approximate eigenstates, in both energy and wave functions, is assessed by comparing the results obtained using two basis sets of different sizes. In our case, we take as the "exact" results, denoted $\mathcal{E}'_N, |N'\rangle$, those obtained variationally by diagonalization in a very large basis set (∼5000 elements) of harmonic oscillator eigenfunctions [1,2].

In Fig. 19 we present such errors for both eigenenergies (bottom) and eigenfunctions (top) of all symmetry classes, computed as $\Delta\mathcal{E}_r = |\mathcal{E}_N - \mathcal{E}_{N'}|\rho$ (measured in mean energy level spacing units of each symmetry class) and $1 - \langle N|N'\rangle^2$, respectively, as a function of the reduced dispersion of the eigenfunctions,

$$\sigma_r = \sigma_N \rho,$$

where σ_N is the dispersion of the eigenfunction $|N\rangle_\chi$. As can be seen, both $\Delta\mathcal{E}_r$ and $1 - \langle N|N'\rangle^2$ follow, to a great degree of accuracy, a power law for $\sigma_r < 0.3$, thus giving upper bounds that can be expressed as

$$\Delta\mathcal{E}_r \leqslant \frac{\sigma_r^{2.5}}{4}, \quad 1 - \langle N|N'\rangle^2 \leqslant \frac{\sigma_r^{2.5}}{100}. \tag{42}$$

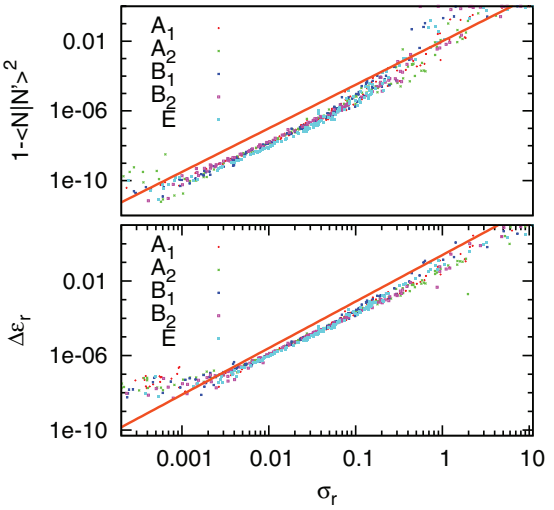

FIG. 19. (Color online) Error in the eigenenergies (bottom) and eigenfunctions (top) of the eigenstates obtained in our calculation using a basis set of scar functions, estimated as described in Sec. IV E, as a function of the relative dispersion, $\sigma_r = \sigma_N \rho$. Solid lines indicate the upper error bounds given in Eq. (42).

There is a good reason for calculating the previous upper bounds as a function of σ_r. Indeed, the latter magnitude can be computed straightforwardly, so that one can estimate the errors in the results with the aid of Eq. (42), without the need for any further calculation. Note that, for very small values of the dispersion, the accuracy of our calculations is dominated by precision errors, and these expressions for the error bounds do not apply.

V. CONCLUSIONS

In this paper, we develop a new method for constructing basis sets from scar functions which are able to calculate very accurately the eigenstates of classically chaotic systems, keeping the problem at very moderate sizes. The main idea is that introducing the relevant dynamical information into the basis elements has a twofold effect. First, the efficiency of the basis set is fostered, and second, its nature allows us a straightforward identification of the underlying classical structures contributing to each individual eigenstate, thus providing a good description of the quantum dynamics in a semiclassical sense.

As an illustration we have applied the method to a classically chaotic quartic two-dimensional oscillator [see Eq. (1)], which has been used as a benchmark in the field of quantum chaos. The performance of our method for this system was superb, since we have demonstrated that the method can be advantageously applied to the computation of excited states in a small energy window using very modest basis sets, whose sizes can be estimated from the average participation ratio. Moreover, using a basis set of ∼2500 elements, we have been able to compute the first low-lying ∼2400 eigenstates with an accuracy, in both energies and wave functions, similar to that of other standard methods used in the past to study the same oscillator.

Furthermore, we have examined the quality of our results using a variety of different indicators, such as projection on local (scar) representations, scar intensities, and participation ratios. The first two allow a direct description of the different

eigenstates in terms of semiclassical ideas, while the latter provides an idea of how our scar basis is much smaller than the other conventional one. Furthermore, we have also provided in this work upper bounds to the errors that can be expected in our calculations, in both energy and wave functions.

We are currently extending the method to realistic molecular systems with a mixed phase space, where the degree of chaos of a trajectory corresponding to some given initial conditions depends on the energy. The results of an application to the LiNC/LiCN isomerizing system will be reported elsewhere.

ACKNOWLEDGMENTS

We thank the referees, whose comments helped to improve the presentation of the paper. This work was supported by MINECO (Spain), under projects MTM2009-14621 and ICMAT Severo Ochoa SEV-2011-0087, and by CEAL Banco de Santander–UAM. F.R. is grateful for the support from a doctoral fellowship from UPM and the hospitality of the members of the Departamento de Física in the Laboratorio TANDAR–Comisión Nacional de la Energía Atómica, where part of this work was done.

[1] R. A. Pullen and A. R. Edmonds, J. Phys. A **14**, L477 (1981); A. Carnegie and I. C. Percival, *ibid.* **17**, 801 (1984); B. Eckhardt, G. Hose, and E. Pollak, Phys. Rev. A **39**, 3776 (1989).

[2] R. L. Waterland, J.-M. Yuan, C. C. Martens, R. E. Gillilan, and W. P. Reinhardt, Phys. Rev. Lett. **61**, 2733 (1988); C. C. Martens, R. L. Waterland, and W. P. Reinhardt, J. Chem. Phys. **90**, 2328 (1989).

[3] M. Brack and R. M. Bhaduri, *Semiclassical Physics* (Addison-Wesley, Reading, MA, 1997).

[4] E. B. Bogomolny, Nonlinearity **5**, 805 (1992).

[5] M. J. Davis and E. J. Heller, J. Chem. Phys. **71**, 3383 (1979); **75**, 3916 (1981); M. Blanco and E. J. Heller, *ibid.* **83**, 1149 (1985).

[6] E. J. Heller, Phys. Rev. Lett. **53**, 1515 (1984).

[7] M. C. Gutzwiller, *Chaos Classical and Quantum Mechanics* (Springer-Verlag, New York, 1990).

[8] L. Kaplan and E. J. Heller, Ann. Phys. **264**, 171 (1998).

[9] E. B. Bogomolny, Physica D **31**, 169 (1988).

[10] M. V. Berry, Proc. R. Soc. Lond. A **423**, 219 (1989).

[11] S. Tomsovic and E. J. Heller, Phys. Rev. Lett. **70**, 1405 (1993); S. Tomsovic and J. H. Lefebvre, *ibid.* **79**, 3629 (1997).

[12] D. A. Wisniacki, E. G. Vergini, R. M. Benito, and F. Borondo, Phys. Rev. E **70**, 035202(R) (2004); Phys. Rev. Lett. **94**, 054101 (2005); **97**, 094101 (2006).

[13] J. P. Keating and S. D. Prado, Proc. R. Soc. London A **457**, 1855 (2001).

[14] D. Wisniacki and G. G. Carlo, Phys. Rev. E **77**, 045201(R) (2008); M. Novaes, J. M. Pedrosa, D. Wisniacki, G. G. Carlo, and J. P. Keating, *ibid.* **80**, 035202(R) (2009).

[15] H. Xu, L. Huang, Y.-C. Lai, and C. Grebogi, Phys. Rev. Lett. **110**, 064102 (2013).

[16] S. Sridhar, Phys. Rev. Lett. **67**, 785 (1991); J. Stein and H. J. Stöckmann, *ibid.* **68**, 2867 (1992).

[17] P. B. Wilkinson, T. M. Fromhold, L. Eaves, F. W. Sheard, N. Miura, and T. Takamasu, Nature (London) **380**, 608 (1996); R. Akis, D. K. Ferry, and J. P. Bird, Phys. Rev. Lett. **79**, 123 (1997).

[18] J. U. Nöckel and A. D. Stone, Nature (London) **385**, 45 (1997); C. Gmachl, F. Capasso, E. E. Narimanov, J. U. Nöckel, A. D. Stone, J. Faist, D. L. Sivco, and A. Y. Cho, Science **280**, 1556 (1998); T. Harayama, T. Fukushima, P. Davis, P. O. Vaccaro, T. Miyasaka, T. Nishimura, and T. Aida, Phys. Rev. E **67**, 015207(R) (2003); Q. H. Song, L. Ge, A. D. Stone, H. Cao, J. Wiersig, J.-B. Shim, J. Unterhinninghofen, W. Fang, and G. S. Solomon, Phys. Rev. Lett. **105**, 103902 (2010); J. Wiersig, A. Eberspächer, J.-B. Shim, J.-W. Ryu, S. Shinohara, M. Hentschel, and H. Schomerus, Phys. Rev. A **84**, 023845 (2011).

[19] V. Doya, O. Legrand, F. Mortessagne, and C. Miniatura, Phys. Rev. Lett. **88**, 014102 (2001); C. Michel, V. Doya, O. Legrand, and F. Mortessagne, *ibid.* **99**, 224101 (2007).

[20] L. Huang, Y.-C. Lai, D. K. Ferry, S. M. Goodnick, and R. Akis, Phys. Rev. Lett. **103**, 054101 (2009).

[21] G. G. de Polavieja, F. Borondo, and R. M. Benito, Phys. Rev. Lett. **73**, 1613 (1994).

[22] E. G. Vergini, J. Phys. A **33**, 4709 (2000); E. G. Vergini and G. G. Carlo, *ibid.* **33**, 4717 (2000).

[23] E. G. Vergini and G. G. Carlo, J. Phys. A **34**, 4525 (2001).

[24] E. L. Sibert III, E. G. Vergini, R. M. Benito, and F. Borondo, New J. Phys. **10**, 053016 (2006).

[25] F. Revuelta, E. G. Vergini, R. M. Benito, and F. Borondo, Phys. Rev. E **85**, 026214 (2012).

[26] A. Vagov, H. Schomerus, and V. V. Zalipaev, Phys. Rev. E **80**, 056202 (2009).

[27] E. G. Vergini, D. Schneider, and A. M. Rivas, J. Phys. A **41**, 405102 (2008).

[28] J. M. Pedrosa, D. Wisniacki, G. G. Carlo, and M. Novaes, Phys. Rev. E **85**, 036203 (2012).

[29] O. Bohigas, S. Tomsovic, and D. Ullmo, Phys. Rep. **223**, 43 (1993).

[30] E. G. Vergini, E. Sibert III, F. Revuelta, R. M. Benito, and F. Borondo, Europhys. Lett. **89**, 40013 (2010).

[31] P. Dahlqvist and G. Russberg, Phys. Rev. Lett. **65**, 2837 (1990).

[32] T. Kapela and C. Simó, arXiv:1105.3235v1.

[33] E. J. Heller, J. Chem. Phys. **65**, 4979 (1976).

[34] R. G. Littlejohn, Phys. Rep. **138**, 195 (1986).

[35] V. A. Yakubovich and V. M. Starzhinskii, *Lineal Differential Equations with Periodic Coefficients* (Wiley, New York, 1975).

[36] S. C. Creagh, J. M. Robbins, and R. G. Littlejohn, Phys. Rev. A **42**, 1907 (1990).

[37] J. M. Robbins, Nonlinearity **4**, 343 (1991).

[38] E. G. Vergini and D. Schneider, J. Phys. A **38**, 587 (2005).

[39] S. Lang, *Algebra* (Springer-Verlag, New York, 2002).

[40] W. H. Press, S. A. Teukolsky, W. T. Vetterling, and B. P. Flannery, *Numerical Recipes in FORTRAN 90* (Cambridge University Press, Cambridge, 1996).

[41] E. G. Vergini, J. Phys. A **37**, 6507 (2004); arXiv:nlin/0205001.

[42] M. V. Berry, J. Phys. A **10**, 2083 (1977).

[43] See Supplemental Material at http://link.aps.org/supplemental/10.1103/PhysRevE.87.042921 for the reconstruction of the different symmetry eigenfunctions in the scar function basis set.

[44] D. T. Colbert and W. H. Miller, J. Chem. Phys. **96**, 1982 (1992).

[45] W. Weibull, J. Appl. Mech.-Trans. ASME **18**, 293 (1951); N. L. Johnson, S. Kotz, and N. Balakrishnan, *Continuous Univariate Distributions*, Vol. 1 (John Wiley & Sons, New York, 1994).

[46] D. K. Sparks and B. R. Johnson, J. Chem. Phys. **125**, 114104 (2006).